Nanofluidic electrokinetics

in quasi-two-dimensional branched U-turn channels

Proefschrift

ter verkrijging van de graad van doctor
aan de Technische Universiteit Delft,
op gezag van de Rector Magnificus prof. dr. ir. J.T. Fokkema,
voorzitter van het College voor Promoties,
in het openbaar te verdedigen op maandag 14 januari 2008 om 12:30 uur

door

Gea Oswah Fatah PARIKESIT

natuurkundig ingenieur,
geboren te Bandung, Indonesie.

Dit proefschrift is goedgekeurd door de promotoren:
Prof. dr. I.T. Young
Prof. dr. Y. Garini

Samenstelling promotiecommissie:

Rector Magnificus	voorzitter
Prof. dr. I.T. Young	Technische Universiteit Delft, promotor
Prof. dr. Y. Garini	Bar-Ilan University (Israel), promotor
Prof. dr. C. Dekker	Technische Universiteit Delft
Prof. dr. H.J. Tanke	Leids Universitair Medisch Centrum
Prof. dr. ir. A. van den Berg	Universiteit Twente
Prof. dr. ir. J. Westerweel	Technische Universiteit Delft
Prof. dr. ir. M.W.J. Prins	Philips Research & Technische Universiteit Eindhoven
Prof. dr. ir. L.J. van Vliet	Technische Universiteit Delft, reservelid

Dit werk maakt deel uit van het onderzoekprogramma van de Stichting voor Fundamenteel Onderzoek der Materie (FOM), die financieel wordt gesteund door de Nederlandse Organisatie voor Wetenschappelijk Onderzoek (NWO).

http://www.library.tudelft.nl/dissertations/

ISBN: 978-90-9022486-2
Copyright © 2008 by Gea Oswah Fatah Parikesit
Printed by Gildeprint Drukkerijen B.V., Enschede www.gildeprint.nl

Samenvatting

Nano-vloeistof electrokinetica in quasi-twee-dimensionaal vertakte U-draai kanalen

De *lab-on-a-chip* (LOC) is een nieuwe technologie die concentreerde zich op het analyseren en controleren van stromen van vloeistoffen, ionen, en (bio) deeltjes op de nanometer en micrometerschalen, die ons toestaan om een volledig vloeistof-gebaseerd laboratorium te krimpen in een muntstuk-grootte instrumentatie. Onder andere toepassingen, de LOC technologie kan worden gebruikt om de elektroforese van DNA op het individuele-molekul-niveau uit te voeren, een belangrijke kwestie in genomische studien en polymeerfysica.

In dit proefschrift, bestuderen wij een nieuw vloeistof-kanaal structuur met "vertakte U-draai" vorm, om zijn potentieel voor grootte-gebaseerde sorteren en kenmerken van individuele DNA molekulen te onderzoeken. De stroom van de vloeistof en de beweging van DNA molekulen binnen de structuur worden met elektrische velden gecontroleerd en met de kwantitatieve fluorescentiemicroscopie geanalyseerd. De kanaaldiepte is minder dan 1 micrometer, terwijl de kanaallengten en breedten zijn rond 100 micrometers. Wegens deze afmetingen, kan de structuur als quasi-twee-dimensionaal systeem worden vereenvoudigd wanneer wij digitale beeldanalyse en numerieke simulatie uitvoeren. Met deze kanalen, stellen wij in **Hoofdstuk 1** de volgende onderzoekkwesties:
1. Hoe gedraagt de stroom van de vloeistof zich wanneer diverse elektrische velden over deze kanalen worden toegepast?
2. Hoe gedragen *pathlines* van de individuele DNA molekulen zich binnen de het beperken nanokanalen?
3. Kunnen wij deze kanalen als nieuwe instrumenten gebruiken om individuele DNA molekulen te sorteren en te kenmerken?

In **Hoofdstuk 2**, herzien wij de concepten van electrokinetica. Dit bestaat uit de electro-osmotische stroom van de vloeistof evenals uit het elektroforetische en dielektroforetische bewegen van deeltjes in de vloeistof. Wij tonen ook belangrijke verschillen in de elektrokinetische fenomenen in micro-vloeistof en nano-vloeistof milieu's. De eigenschappen van de DNA molekulen als polyelektrolyten worden ook besproken. Wij beschrijven ook het gebruik van kwantitatieve optische beeldvorming, in de vorm van fluorescentiemicroscopie, om electrokinetica binnen mikro-kanalen te onderzoeken.

Hoofdstuk 3 beschrijft de nano-kanalen die in dit onderzoek worden bestudeerd. Wij beginnen door het ontwerp van de vertakte U-draai nano-kanalen, met het doel om individuele DNA molekulen te sorteren en te kenmerken. De vervaardigingsstappen van het kanalen-op-*chip* worden ook beschreven. Wij gaan dan met het ontwerp en de vervaardiging van een *interface*, die wij gebruiken om

de nano-kanalen aan externe instrumentatie aan te sluiten. Blijvende uitdagingen die in het vervaardigingsproces bestaan en het experimentele onderzoek beïnvloeden ook worden beschreven.

In **Hoofdstuk 4** bestudeerden wij de eerste onderzoekkwestie door de electro-osmotische stroom binnen de nano-kanalen te onderzoeken en te analyseren. In de experimenten, gebruiken wij gedistilleerd water als vloeistof waarin wij fluorescente deeltjes met een diameter van 110 nanometer toevoegen die als traceur-deeltjes worden gebruiken binnen nano-kanalen met een diepte van 150 nanometer. Van de resultaten kunnen wij de *pathlines* en de snelheidsdistributie van de vloeibare stroom kenmerken. Wegens de complexe vorm van het kanaal, kan de electro-osmotische stroom niet analytisch gerekend worden. Daarom gebruiken wij numerieke stroomsimulaties om ons model te bouwen. De vergelijking tussen de experimentele gegevens en de simulatieresultaten geeft een zeer goede overeenkomst, waar de afwijking kan verklaard worden door de gemeten Brownbeweging van de traceur-deeltjes, die in de simulatie was niet opgenomen.

De tweede onderzoekkwestie werd onderzocht in **Hoofdstuk 5**. De experimenten worden uitgevoerd met twee soorten dsDNA-molekulen, λ (48.5 kbp) en T4GT7 (165.6 kbp), in kanalen met diepte van 400 nanometer. Wij merken op dat elektrokinetische *pathlines* van de DNA molekulen hangt van de grootte van elk DNA af. Wij gebruiken numerieke simulatie om de distributie van elektrokinetische krachten in de kanalen te berekenen, die de waargenomen experimentele fenomenen kunnen verklaren. De resultaten van Hoofdstuk 5 wijzen er ook op dat, voor het eerst, de op grootte-gebaseerde scheiding van DNA molekulen in ononderbroken en zonder-zeef manier kan worden gedaan. Dit is verwant met onze derde onderzoekkwestie. Door de nano-kanaal-vorm te gebruiken, kunnen wij het elektrische veld distributie in de kanalen vormen en de elektrokinetische krachten manipuleren om *pathlines* van de DNA molekulen te beïnvloeden. De zelfde resultaten kunnen niet alleen op de DNA molekulen worden verwacht, maar ook op al andere polariseerbaar biologische molekulen die kunnen worden gemanipuleerd met dielektroforese.

De algemene overzichten op de resultaten, samen met sommige aanbevelingen, worden gegeven in **Hoofdstuk 6**.

Gea Oswah Fatah PARIKESIT, Delft, January 2008

Summary

Nanofluidic electrokinetics in quasi-two-dimensional branched U-turn channels

Lab-on-a-Chip (LOC) is a new technology focused on analyzing and controlling flows of fluids, ions, and (bio) particles on the nanometer and micrometer scales, allowing us to shrink a complete fluid-based laboratory into a coin-sized instrumentation. Among other applications, LOC technology can be used to perform DNA electrophoresis on the single-molecule level, an important issue in genomic studies and polymer physics.

In this thesis, we study a novel fluidic structure with a "branched U-turn" geometry, investigating its potential to perform size-based sorting and characterization on DNA single-molecules. The fluid flow and the DNA molecule motion within the fluidic structure are controlled using electric fields and analyzed with quantitative fluorescence microscopy. The channel depth is less than 1 micrometer, while the channel lengths and widths are in the range of 100 micrometers. Due to these dimensions, the fluidic structure can be simplified as a quasi-two-dimensional system when we perform digital image analysis and numerical simulation. Using these channels, in **Chapter 1** we pose the following research questions:

1. How does the fluid flow behave when various types of electric fields are applied across these channels?
2. How do the pathlines of individual DNA molecules behave inside the confining nanofluidic channels?
3. Can we use these channels as novel devices to sort and characterize single DNA molecules?

In **Chapter 2**, we review the concepts of electrokinetics. This comprises the electro-osmotic flow of the fluid as well as the electrophoretic and dielectrophoretic motion of particles in the fluid. We also show important differences in the electrokinetic phenomena in microfluidic and nanofluidic environments. The properties of DNA molecules as polyelectrolytes are also discussed. Furthermore, we describe the use of quantitative optical imaging, particularly using fluorescence microscopy, for investigating electrokinetics in microfabricated channels.

Chapter 3 describes the nanofluidic channels studied in this research. We start by explaining the design of the branched U-turn nanofluidic channels, with the goal of sorting and characterizing DNA molecules. The fabrication steps of the channels-on-chip are also described. We then proceed with the design and fabrication of an interface, which we use to connect the nanofluidic chips to external instrumentation. Persistent challenges that exist in the fabrication process and influence the course of the experimental research are also described.

In **Chapter 4** we studied the first research question by investigating and analyzing the electro-osmotic flow inside the nanofluidic channels. In the experiments, we use distilled water as the liquid in which we add 110 nm diameter fluorescent beads employed as tracer-particles inside 150 nm deep nanofluidic channels. From the results we can characterize the pathlines and velocity distribution of the fluid flow. Due to the complex geometry of the channel, the electro-osmotic flow cannot be calculated analytically. Therefore we use numerical flow simulations to build our model. Comparison between the experimental data and the simulation results give a very good agreement, where the deviation can be explained by the measured Brownian motion of the tracer-particles which was not incorporated in the simulation.

The second research question was investigated in **Chapter 5**. Experiments are performed with two types of dsDNA molecules, λ (48.5 kbp) and T4GT7 (165.6 kbp), using channels with depth of 400 nm. We observe that the electrokinetic pathlines of the DNA molecules depends on the DNA size. We use numerical simulation to calculate the distribution of electrokinetic forces in the channels, which can explain the observed experimental phenomena. The results of Chapter 5 also indicate that, for the first time, size-based separation of DNA molecules can be done in a continuous, sieve-less, manner. This is related to our third research question. By using the nanofluidic channel geometry, we can configure the electric field distribution in the channels and manipulate the electrokinetic forces to influence the pathlines of the DNA molecules. The same results can be expected not only on DNA molecules, but also on any other polarizable biological molecules that can be manipulated using dielectrophoresis.

General reviews on the results, along with some recommendations, are given in **Chapter 6**.

Gea Oswah Fatah PARIKESIT, Delft, January 2008

Table of Contents

I. Life in a nanofluidic world........1
  I.1 Nanofluidic phenomena........1
  I.2 Nanofluidics and Lab-on-a-Chip........3
  I.3 Scope of this thesis........5

II. Electrokinetics in microfabricated channels........9
  II.1 The electric double layer........9
  II.2 The flow of liquids and ions........11
  II.3 Electro-osmosis........13
  II.4 Electrophoresis........14
  II.5 Dielectrophoresis........15
  II.6 From microfluidics to nanofluidics........16
  II.7 DNA as polyelectrolytes........18
  II.8 Quantitative optical imaging........19

III. Quasi-2D branched U-turn nanofluidic channels........23
  III.1 The geometry of the nanofluidic channels........23
  III.2 Fabrication of the channels-on-chips........25
  III.3 An interface for the channels-on-chips........26
  III.4 Epilogue: Problems with the embedded electrodes........28

IV. Electro-osmotic flow analysis of a branched U-turn nanofluidic channel........29
  IV.1 Introduction........29
  IV.2 Analysis methods........32
  IV.3 Results and discussion........37
  IV.4 Conclusions........42

V. Size-dependent electrokinetic pathlines of DNA molecules in sieve-less U-turn nanochannels........43
  V.1 Introduction........43
  V.2 Methods........44
  V.3 Results and discussions........47
  V.4 Conclusion........56
  V.5 Epilogue........56

VI. General conclusions 59
  VI.1 Review of results 59
  VI.2 Recommendations 60

References 63
List of symbols 69
Acknowledgements 71
Curriculum Vitae 72

I. Life in a nanofluidic world

I.1 Nanofluidic phenomena

Nanofluidics describes the phenomena of fluids, which comprise liquids and gases, at the nanometer scale. These phenomena can be found abundantly in nature [*Eijkel et al., 2005*]. For example, the cells that build our bodies work in a nanofluidic environment. Another example is the self-cleaning 'Lotus effect', where interactions between water and nanometer structures on the surfaces of Lotus leaves allow raindrops to roll off and take dust particles and micro-organisms away from the leaves.

Nanofluidic phenomena are not just *smaller* than fluidic phenomena at larger scales, but also *different*, and frequently seem counter-intuitive to us. To quantitatively portray one example of those differences, we can look at one particular dimensionless number: the Reynolds number, *R*. It is defined as:

$$R = \frac{\rho u^2 / l}{\mu u / l^2} = \frac{\text{inertial forces}}{\text{viscous forces}} = \frac{\rho u l}{\mu} = \frac{u l}{\nu} \ , \qquad (1.1)$$

with ρ as the fluid density, u the bulk fluid velocity, l the characteristic length in the system, μ the dynamic fluid viscosity, and ν the kinematic fluid viscosity ($\nu = \mu/\rho$). At the nanometer scale, where the value of l is very small, the Reynolds number also becomes very small. Consequently, the inertial forces become negligible compared to the viscous forces. In 1976, E.M. Purcell gave an enlightening talk on how we would live in a world with a very small Reynolds number [*Purcell, 1977*]. The significant viscous forces dictate that we would move as if we are immersed in highly viscous syrup, such that swimming would be an immensely hard task to perform. Any swimming style that uses reciprocal motion (that is, where we change our body shape into another shape, and then we go back to the original shape by going through the sequence in reverse) would be rendered useless at a very small Reynolds number, and we would not go anywhere because we have no inertial forces to use. The bacteria *E. coli* solve this problem by performing a type of non-reciprocal motion: their tails (which are called *flagella* and have a diameter of approximately 13 nm) are shaped as a helix and turn continuously around a rotary joint [*Purcell, 1977*]. This continuous turn, which is analogous to the motion of a corkscrew, eventually propels the bacteria in one particular direction.

Another important difference arises as we shift from large-scale fluidics to nanofluidics, namely the increasing importance of surface-effects as compared to bulk-effects. Imagine a volume of fluid confined by the walls of a solid cube. In large-scale fluidics, only the parts of the fluid in the vicinity of the walls are significantly influenced by the existence of the cube, while the other parts are not.

When the characteristic length of the cube is reduced to the nanometer scale, however, the confining walls influence most parts of the fluid. As the characteristic length is reduced, the surface-to-volume ratio gets higher, and the interfaces surrounding the volume of fluid become more important. The behaviour of fluids at interfaces is characterized by the surface tension, γ. The rising of water along a capillary column, for instance, can be explained by the surface tension in the water-air-solid interfaces. The pressure difference induced by the surface tension can reach more than ~10 bar for a capillary diameter of 100 nm [*Eijkel et al., 2006b*]. Hence if a liquid touches the entrance of a nanofluidic capillary, the liquid will spontaneously fill the capillary, assuming the capillary surfaces are not hydrophobic.

As the surface-effects become more dominant, the slip of fluid flows at the walls could also become more significant. For flows inside channels with dimensions larger than 1 mm, this slip can be considered negligible, and the assumption of no-slip at the walls remains valid. When we have fluidic channels with dimensions of micrometers and nanometers, however, the length of this slip may be in the same order as the channel dimensions. In particular, a slip length of 1 μm has been reported at hydrophobic microfluidic channel walls [*Tretheway et al., 2002*].

Another important surface-effect originates in the existence of ions at the solid-liquid surfaces. The solid surfaces generally have a certain surface charge, caused by ionization processes [*Probstein, 2003*]. This effect is very important in a nanofluidic environment, for example in biological cells, where ions and surfaces are ubiquitous. A gradient of electrical potential induces motions of the ions, which in turn drives the transport of fluid and objects. These electrical-driven transport phenomena are called *electrokinetics*.

Nanometer-scale objects also behave differently than their large-scale counterparts. Due to the very small dimensions, gravitational forces on (and sedimentation of) such objects are negligible. As examples, the gravitational forces acting on a 1 mm^3 cube of water and a 1 nm^3 cube of water are 9.8×10^{-6} N and 9.8×10^{-24} N, respectively, assuming earth gravity of 9.8 m/s^2 and water density of 1000 kg/m^3. On the other hand, the Brownian motion becomes much more significant. This motion is a random movement of small objects due to the constant bombardment from the thermally excited liquid molecules surrounding them. The Brownian motion causes diffusion of particles, and for a spherical particle this is usually quantified using the diffusion constant defined as $D=(k_b * T)/(6 * \pi * \mu * a)$, where k_b is the Boltzmann constant, T is the absolute temperature, and a is the particle diameter. Due to the combination of the Brownian motion and the low Reynolds number in nanofluidics, mixing of two liquids inside nanofluidic environments depends strongly on diffusion rather than on inertial forces (e.g. by stirring the liquids).

To get more insight into the nanofluidic phenomena, one should read the excellent review paper by J.C.T. Eijkel and A. v.d.Berg [*Eijkel et al., 2005*]. The micrometer-scale counterparts of these phenomena, known as microfluidics, are described in the review paper by T.M. Squires and S.R. Quake [*Squires et al., 2005*].

I.2 Nanofluidics and Lab-on-a-Chip

Nanofluidic environments do not only exist in nature. They can also be artificially fabricated using micro-fabrication methods, which have been developed and used to produce silicon-based integrated electronic circuits. The resulting technology is known as Lab-on-a-Chip (LOC).

In LOC technology, nanofluidic and microfluidic channels are fabricated on a single microchip. These channels can also be equipped with various embedded sensors and actuators, thus forming devices and instrumentations at the nanometer and micrometer scales. In principle, the LOC technology allows us to shrink a complete fluidic-based laboratory onto a single chip.

Major advantages of this technology are the following:

- Due to the low volume of the fluidic channels, only a low volume of sample and analyte is consumed, which in turn results in less cost. These materials produce a low volume of reactants and wastes, which results in safer and more controlled experiments.
- Fast and repeatable experiments are feasible because many processes can be automated and performed in parallel on the same microchip.
- The small size of the microchip, combined with the possibility of interfacing the microchip to external instrumentation, allows for portability so that experiments can be done almost anywhere and anytime, including at resource-poor locations.
- Because the fabrication of the microchip is based on the mature microelectronics fabrication technology, lower fabrication costs can be achieved, allowing for mass production of disposable microchips.

Hence the LOC technology offers new possibilities for basic research as well as for applications in the fields of chemistry, biology, biotechnology, and medical engineering. Several investigators started this technology, including Manz et al. who published their seminal paper in 1990, dubbing the concept as MicroTAS (micro total analysis systems) [*Manz et al., 1990*]. As it became clear that this concept could be used for more than analysis purposes, the term Lab-on-a-Chip became common to provide a more general description. A new research field eventually became established around this technology. An overview of the conference series MicroTAS, which was started in 1994 in Enschede, The Netherlands, shows that nanofluidics and microfluidics are the essential generic phenomena that drive the LOC technology [*van den Berg et al., 2006*].

Even though this new technology is very promising, it provides challenges for the researchers aiming to utilize it [*Whitesides, 2006*]. The most important challenge arises from the fact that the phenomena of microfluidics and nanofluidics are different from the fluidic phenomena at larger scales, as discussed in the previous section. This prevents researchers from simply downsizing existing conventional-sized devices to nanofluidic and microfluidics devices, as they do not work in exactly the same way.

One important application of the LOC technology is for sorting and characterizing DNA (*deoxyribonucleic acid*) molecules. The genetic information in DNA molecules, which forms the basis for all biological species activities and hereditary mechanisms, is required for various applications, ranging from medical diagnosis to forensic identification. To obtain this information, the sequence of nucleotides (*adenine*, *thymine*, *cytosine*, and *guanine*) comprising the DNA molecules needs to be identified. One way to accomplish this task, known as genome sequencing, is by breaking the DNA molecules into smaller pieces with different lengths, and subsequently sorting and characterizing each piece according to its length [*Pratt and Cornely, 2004*].

Micro-fabricated periodic constrictions from silicon or polymeric materials have been fabricated inside nanofluidic and microfluidic channels, thus serving as artificial sieves. As DNA molecules are electrokinetically transported through those sieves, they can be sorted because the longer DNA molecules move forward slower than the shorter ones [*Viovy, 2000*]. One example of this approach is the so-called DNA-prism device described by Huang et al. [*Huang et al., 2002*]. Another approach with artificial periodic constrictions uses the entropic behaviour of DNA molecules [*Cabodi et al., 2002*; *Han et al., 1999*].

LOC technology also allows for a better-controlled manipulation and characterization of DNA at the *single-molecule* level because the length scale of the fluidic channels can coincide with the length scale of the DNA molecules [*Tegenfeldt et al., 2004*]. The sorting and characterization of single DNA molecules are particularly useful because they reveal the properties and behaviours of each individual molecule, which are usually hidden if we perform conventional measurements on ensembles of molecules. The knowledge acquired in such studies is useful not only in the field of genomics, but also in polymer physics. As polymers, the DNA molecules serve as the “ideal macromolecules”: they are available in nature in mono-dispersed size distributions and in a wide size range (from one basepair to hundreds of Mega-basepairs) [*Viovy, 2000*].

Generally, in applying LOC technology to perform single-molecule studies, researchers need to perform two different tasks: (1) confining and manipulating the biological molecules (in liquid solution) inside microfabricated channels, and (2) detecting and characterizing the behaviour and properties of the molecules and the fluid flow [*Tegenfeldt et al., 2004*]. Nanofluidics is very promising in executing both tasks.

In biomolecular confinement and manipulation, nanofluidics could provide novel and useful methods. In channels with depths at the nanometer scale, new and exciting separation mechanisms have been reported [*Garcia et al., 2005*; *Pennathur et al., 2005*], which could also be applied to single-molecule DNA sorting. Meanwhile, in biomolecular detection and characterization, the extra confinement provided by nanofluidic channels allows for smaller optical focal volume, which in turn allows for single-molecule detections even in high molecule concentrations [*Foquet et al., 2004*]. Combining nanofluidics, microfluidics, and quantitative optical fluorescence microscopy opens the way into detection and imaging of single DNA molecules [*Dittrich et al., 2005*]. The resulting image sequences can then be processed and analysed in many ways, among others by using particle tracking velocimetry [*Sinton, 2004*]. This method specifically allows us to characterize the dynamics of the single-molecules flowing inside the nanofluidic channels and devices, while it also enables us to visualize and analyse the flow of the fluid itself.

I.3 Scope of this thesis

In LOC-based DNA sorting and characterization, the DNA sample is typically injected through a cross-junction or a pair of T-junctions, such that a narrow and well-defined sample band is formed before the sample is separated along a straight separation channel (see Figure 1.1). To make the separation length sufficiently long while keeping the channel length sufficiently short, the separation channel can also be shaped as a serpentine-like channel, where several straight channels are connected in series using U-turns. Major disadvantages usually caused by a U-turn are sample dispersion and separation degradation in the so-called “race-track” effect, where sample flowing along the inner radius moves faster than sample flowing along the outer radius.

We investigate the possibility of eliminating these disadvantages by using U-turn channels as the *main separation channels* themselves, thus *not* just as connectors between straight channels. When separation is performed *across* the channel width, instead of *along* the channel length as typically done, two advantages can be gained from the U-turn channel: (1) the “race-track” effect will not influence the separation quality to any significant extent, and (2) biomolecular separation could be run continuously, allowing for high-throughput analysis and avoiding the requirement of a narrow and well-defined sample band.

We study therefore novel nanofluidic channels with a ”branched U-turn" geometry. The fluid flow and the DNA molecule motion within the channels are controlled using applied electric fields and analyzed with quantitative fluorescence microscopy. The channel depth is less than 1 micrometer, while the channel lengths and widths are in the range of 100 micrometers. Due to these dimensions, the nanofluidic channels can be described as a quasi-two-dimensional system.

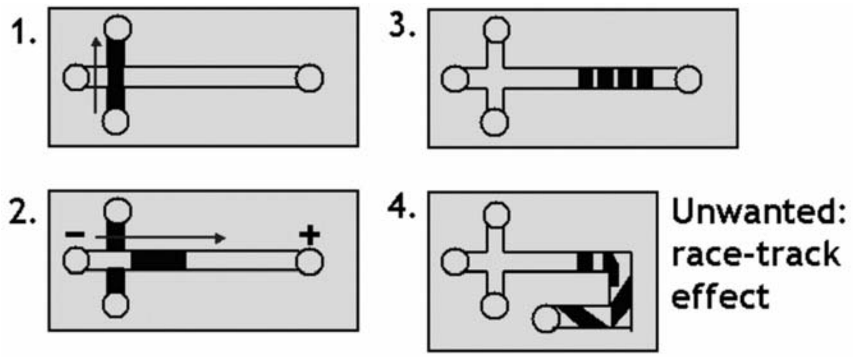

Figure 1.1 Typical steps in LOC-based DNA sorting and characterization methods: (1) sample injection through a cross junction; (2) transport of a sample band through the long separation channel; (3) DNA fragments in the sample are separated and form new bands along the channel length; (4) in case the separation channel is not sufficiently long, U-turns can be used to effectively lengthen the separation channel (this, however, results in unwanted race-track effect; see text for detailed discussion).

Using these quasi-two-dimensional branched U-turn nanofluidic channels, we pose the following research questions:

1. How does the fluid flow behave when various types of electric fields are applied across these channels?
2. How do the pathlines of individual DNA molecules behave inside the confining nanofluidic channels?
3. Can we use these channels as novel devices to sort and characterize single DNA molecules?

In **Chapter 2**, we review the concepts of electrokinetics. This comprises the electro-osmotic flow of the fluid as well as the electrophoretic and dielectrophoretic motion of particles in the fluid. We also show important differences in the electrokinetic phenomena in microfluidic and nanofluidic environments. The properties of DNA molecules as polyelectrolytes are also discussed. We also describe the use of quantitative optical imaging, particularly using fluorescence microscopy, for investigating electrokinetics in microfabricated channels.

Chapter 3 describes the nanofluidic channels studied in this research. We start by explaining the design of the branched U-turn nanofluidic channels, with the goal of sorting and characterizing DNA molecules. The fabrication steps of the channels-on-chip are also described. We then proceed with the design and fabrication of an interface, which we use to connect the nanofluidic chips to external instrumentation. Persistent challenges that exist in the fabrication process, and influence the course of the experimental research, are also described.

Chapter 4 gives an electro-osmotic flow analysis of the nanofluidic channels. Using fluorescent beads as tracer-particles, diluted in distilled water, we characterize the pathlines and velocity distribution of the electro-osmotic flow in the channel. Because our channel geometry is complex, an analytical solution cannot be used to model the system, and we therefore use numerical flow simulation for the analysis. The analysis shows the important influence of Brownian motion on the pathlines and velocity distribution.

In **Chapter 5**, we investigate the electrokinetic pathlines of DNA molecules in the nanofluidic channels using two types of dsDNA molecules, λ (48.5 kbp) and T4GT7 (165.6 kbp), where the channel depth is 400 nm. We observe that the pathlines of the molecules depends on the DNA size, particularly near regions with high electric field gradient. We use numerical simulation to calculate the distribution of electrokinetic forces in the channels. Our results indicate that, for the first time, size-based separation of DNA molecules could be done in a continuous, sieve-less, manner.

General reviews on the results, along with some recommendations, are given in **Chapter 6**.

II. Electrokinetics in microfabricated channels

II.1 The electric double layer

When a liquid fills a microfabricated channel, an interface is formed between the solid channel walls and the liquid. The solid channel walls generally carry electrostatic surface charges caused by ionization, ion adsorption, ion dissolution, or other charging mechanisms [*Li, 2004*; *Probstein, 2003*]. The liquid itself generally contains positive and negative ions. When the liquid is electrically neutral, the numbers of positive and negative ions are equal. The ions in the liquid that have charges opposite to the walls surface charges are called *counter-ions*, while the ions with charges like the walls surface charges are called *co-ions*. The surface charges on the walls attract the counter-ions and repel the co-ions, as illustrated in Figure 2.1.

The counter-ions attraction, the co-ions repulsion, and the random thermal motion of all the ions in the liquid, cause the formation of the so-called *electric double layer* (EDL). The characteristic thickness of the EDL is given by the inverse of the Debye-Huckel parameter [*Li, 2004*]:

$$\frac{1}{\kappa}=\left[\frac{\varepsilon\varepsilon_0 k_b T}{2Z^2e^2n_\infty}\right]^{1/2}, \qquad (2.1)$$

with κ as the Debye-Huckel parameter, ε the relative permittivity of the liquid solution, ε_0 the permittivity of vacuum, k_b the Boltzmann constant, T the absolute temperature, Z the absolute value of the ionic valence, e the charge of an electron, and n_∞ the ionic number concentration of the bulk liquid. The bulk ionic number concentration is determined by the salt molarity in the fluid, M, i.e.: $n_\infty = N_a * M$, with N_a the Avogadro number (6023×10^{23} kmol^{-1}) and M in [kmol/m^3]. Equation (2.1) shows that the EDL thickness gets larger as n_∞ gets smaller (i.e. when the number of ions in the liquid decreases).

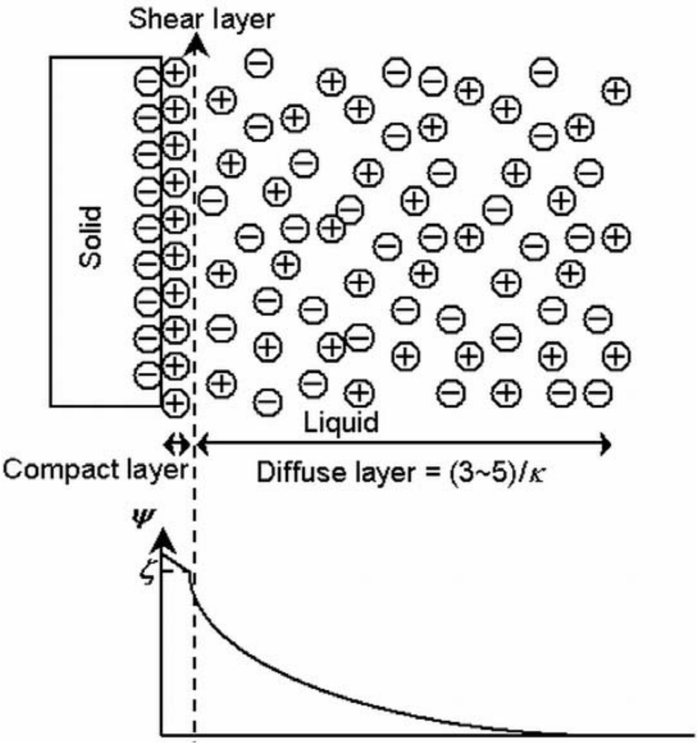

Figure 2.1 The ion concentration distribution (above) and the electric potential distribution (below) in an electric double layer, for an interface between a flat solid surface (with negative surface charges) and an aqueous solution, as a function of distance from the interface toward the solution [*Li, 2004*]. The exponential decay of the electrical potential can usually be calculated using equations (2.2) and (2.3).

The EDL consists of two parts: the compact layer and the diffuse layer. The compact layer is located immediately next to the walls surface, with a thickness of several Angstroms, where counter-ions are immobilized. Further away from the walls, we have the diffuse layer, where the local net charge (i.e. the difference between the charge concentrations of counter-ions and co-ions in that specific location) gradually goes to zero. The boundary between the compact layer and the diffuse layer is usually referred to as the shear layer.

In the liquid, the electric potential distribution is described by the Poisson equation [*Probstein, 2003*]:

$$\nabla^2\psi = -\frac{\rho_e}{\varepsilon\varepsilon_0} , \qquad (2.2)$$

with ψ the local electric field potential in the liquid and ρ_e the local net charge density. It is difficult to measure the electric potential at the solid-liquid interface.

Therefore this parameter is usually approximated by the so-called *zeta potential* (ζ), defined as the electric potential at the shear plane, which can be measured experimentally. Meanwhile, the distribution of ions near the charged walls is given by the Boltzmann distribution [*Probstein, 2003*]:

$$n_i = n_\infty \exp\left[-\frac{Z_i e\psi}{k_b T}\right], \qquad (2.3)$$

with n_i the ionic number concentration of ions of type *i* (i.e. n_+ or n_-) and Z_i the absolute value of the ionic valence of ions type *i*. The ion concentration distribution given by equation (2.3) is derived based on the following assumptions [*Li, 2004*]:

- The system is in equilibrium, i.e. no convection and diffusion.
- The surface charges of the walls are homogeneous.
- The bulk liquid is sufficiently large such that at the center of the channels ψ is equal to zero and n_i is equal to n_∞.

II.2 The flow of liquids and ions

When an incompressible continuous liquid (e.g. water or aqueous electrolyte solutions) inside a channel is set in motion, using either a hydrostatic pressure difference or an electric voltage difference across the ends of the channel, the liquid flow can be described using the Navier-Stokes equation [*Probstein, 2003*]. In this equation, an additive term should be included to take into account the ions in the fluid. As the result, the governing equations of the liquid flow are the continuity equation

$$\nabla.\mathbf{v} = 0 \qquad (2.4)$$

and the momentum equation

$$\rho\left(\frac{\partial \mathbf{v}}{\partial t} + (\mathbf{v}.\nabla)\mathbf{v}\right) = -\nabla P + \mu\nabla^2\mathbf{v} + \rho_e \nabla V, \qquad (2.5)$$

where **v** is the liquid velocity vector, ρ the liquid density, *t* time, *P* the hydrostatic pressure, μ the dynamic fluid viscosity, and *V* the electric voltage.

We can apply a hydrostatic pressure difference between the ends of a channel to induce a liquid flow. When we do this, the ions in the liquid (particularly in the diffuse layer of the EDL) will also flow along the direction of the liquid flow, i.e. flowing downstream. This induced ion flow is called the *streaming current*. Due to the streaming current, we will have more counter-ions in the downstream end than in the upstream end, causing an electrical potential difference between the channel ends. This induced potential difference is called the *streaming potential*. Eventually, the streaming potential will also induce a new flow of ions, called the *conduction current*, where counter-ions flow upstream. The conduction current also induces a new liquid flow in the upstream direction, which is against the direction of the original liquid flow. As the result, the observed liquid flow rate going downstream becomes reduced, giving an impression of a higher viscosity of the liquid. This observed increase of viscosity is usually called the *electro-viscous effect*.

Under a hydrostatic pressure difference, the liquid flow must overcome a *flow resistance* from the fluidic channel. The flow resistance is defined as the ratio between the pressure difference and the liquid flow rate along the channel. In general, for channels with smaller cross-sectional area, the flow resistance of the channel becomes higher. Different cross-sectional geometry with equal cross-sectional area, however, results in different flow resistance. Hence a parameter called hydraulic diameter, D_h, is usually used: $D_h=(4*Area)/(Perimeter)$. Using a pressure difference to transport liquids inside nanofluidic channels can therefore become practically difficult, because of the very small dimensions of the channels.

We can also induce a liquid flow by applying an electrical potential difference between the ends of a channel. The electric field caused by the potential difference drives the ions in the EDL's diffuse layer. Due to the viscosity of the liquid, the flow of the ions also induces the flow of the bulk liquid.

In LOC technology, the electrically driven method is sometimes preferred over the pressure-driven method for actuating the liquid flow and the particle motion. One reason for this preference is because microelectrodes are easier to integrate into the microchips and are mechanically more durable than the moving-mechanics required for pressure-driven actuations. Another reason is the difference between the *flow profiles* of pressure-driven flows and electrically driven flows. The pressure-driven flow profile has a parabolic profile across the channel [*Landau and Lifshitz, 2004*]. When being used to transport particles along the channel, this parabolic profile can become a problem, particularly if the particles in the channel (which can be located anywhere across the cross-section of the channel) are required to flow with a uniform velocity. Meanwhile, the electrically driven flow profile can be made nearly uniform across the channel cross-section [*Li, 2004*]. The velocity gradient in the electrically driven flow profile only occurs inside the EDL's diffuse layer. So by making the EDL much thinner than the channel cross-sectional area, we can make the flow profile almost uniform.

The application of electric fields to drive the motion of fluids and particles is usually referred to as *electrokinetics*. Adopting electrokinetics in LOC technology is very attractive because precise manipulation of very small amounts of fluids and biological molecules can then be performed using either microelectrodes or nanoelectrodes embedded inside the microchips or external electrodes interfacing the microchips to the macro-world instrumentation. The following sections describe three electrokinetic phenomena that are usually employed in LOC technology: electro-osmosis, electrophoresis, and dielectrophoresis.

II.3 Electro-osmosis

Electro-osmosis is the flow of liquids, relative to a stationary charged solid surface, under an electric field [*Probstein, 2003*]. To derive the governing equations in electro-osmosis, we start by substituting ρ_e from the Poisson equation (2.2) into the liquid flow momentum equation (2.5). In nanofluidic channels, the Reynolds number is typically very low, so the liquid motion becomes steady (i.e. ($\partial\mathbf{v}/\partial t$)=0) and the non-linear convection acceleration becomes negligible (i.e. ($\mathbf{v}.\nabla$)$\mathbf{v}$=0). Therefore, when there is no hydrostatic pressure difference between the ends of the channel (∇P=0), the momentum equation (2.5) becomes:

$$0 = \mu\nabla^2\mathbf{v} - \left(\varepsilon\varepsilon_0\nabla^2\psi\right)\mathbf{E} \ , \qquad (2.6)$$

where **E** is the local electric field vector, induced by the electric voltage difference between the ends of the channel.

For the particular case where the channel depth is constant, **E** is not a function of the channel depth; we can then approximate the momentum equation (2.6) of a three-dimensional channel by a two-dimensional channel. Equation (2.6) then becomes:

$$\mu\frac{\partial^2\mathbf{v}(x,y,z)}{\partial z^2} = \left(\varepsilon\varepsilon_0\nabla^2\psi\right)\mathbf{E}(x,y) \ , \qquad (2.7)$$

with z as the Cartesian coordinate axis along the channel depth, while x and y are the Cartesian coordinate axis along the channel lengths and the channel widths. The momentum equation (2.7) can be integrated along the channel depth using the following boundary conditions: $\partial\mathbf{v}/\partial z$=0 and $\partial\psi/\partial z$=0 at the channel walls. This gives:

$$\mu\frac{\partial\mathbf{v}}{\partial z} = \varepsilon\varepsilon_0\frac{\partial\psi}{\partial z}\mathbf{E} \ . \qquad (2.8)$$

Equation (2.8) can be integrated once again along the channel depth, with the boundary conditions of ψ=ζ and $\mathbf{v}(z)$=0 at the channel walls, resulting in:

$$\mathbf{v}_{EO}(x,y,z) = \left(\frac{\varepsilon\varepsilon_0}{\mu}\right)\left(\psi(z) - \zeta\right)\mathbf{E} \ . \qquad (2.9)$$

To fully solve for $\mathbf{v}_{EO}$ (*electro-osmotic velocity*) given by equation (2.9), we first need to solve for $\psi(z)$ in the Poisson equation (2.2). If the Boltzmann distribution in equation (2.3) is valid, we can use it to help solve the Poisson equation (2.2). The combination of the Poisson equation (2.2) and the Boltzmann equation (2.3) is known as the *Poisson-Boltzmann* equation. For a symmetric electrolyte (i.e. where the cations and anions have the same value of z), the Poisson-Boltzmann equation becomes [*Li, 2004*]:

$$\frac{\partial^2 \psi(z)}{\partial z^2} = \left(\frac{2n_\infty Ze}{\varepsilon\varepsilon_0} \right) \sinh\left(\frac{Ze\psi(z)}{k_b T} \right) . \qquad (2.10)$$

From the equation (2.9), we can see that the average value of $\mathbf{v}_{EO}$ (averaged over the channel depth) is linearly proportional to **E**, everywhere along *x* and *y*. For the special case where the EDL thickness is much less than channel depth, the average value of $\mathbf{v}_{EO}$ across the channel depth is expressed by the so-called *Helmholtz-Smoluchowski* equation [*Probstein, 2003*]:

$$\mathbf{v}_{EO\ \mathrm{avg,z}}(x,y) = -\left(\frac{\varepsilon\varepsilon_0\zeta}{\mu} \right) \mathbf{E}(x,y) \ . \qquad (2.11)$$

II.4 Electrophoresis

Electrophoresis is the motion of charged particles or molecules, relative to a stationary ionic liquid, under an applied electric field [*Probstein, 2003*]. When a solid particle is immersed in an ionic liquid, an EDL will also form at the solid-liquid interface.

When we apply an electric field around a particle, both the charged particle and the group of counter-ions surrounding the particle are set in motion. The direction of the particle motion will be opposite to the direction of the motion of counter-ions in the EDL. This opposite directions results in the particle motion being retarded, usually known as *electrophoretic retardation*. This retardation becomes significant when the EDL thickness is neither much larger nor much smaller than the particle size. In general, the electrophoretic velocity is therefore expressed as:

$$\mathbf{v}_{EP,\mathrm{finite\ EDL}} = F\,\frac{2}{3}\left(\frac{\zeta\varepsilon\varepsilon_0}{\mu} \right) \mathbf{E} \ , \qquad (2.12)$$

where *F* is the *Henry function* (a dimensionless number which is a function of the ratio between r_p and $1/\kappa$) that goes to 1 and 3/2 for the thick-EDL and thin-EDL cases, respectively [*Probstein, 2003*].

Let us consider the particular case of a spherical non-conducting particle with negative surface charges. Because the particle is non-conducting, there is electric field lines going through the particle, so on the particle surfaces we have grad(**E**)=0. On one hand, if the EDL thickness is much larger than the particle size (referred above as the thick-EDL case), then the particle can be considered as a point charge in an unperturbed electric field. When the motion equilibrium is reached, the *electrophoretic force* is equal to the Stokes drag force [*Probstein, 2003*]:

$$q_p \mathbf{E} = 6\pi\mu r_p \mathbf{v}_{EP} \ , \qquad (2.13)$$

where q_p is the net charge between the particle and the counter-ions in its EDL, and r_p is the particle radius. Combining equation (2.12) with the surface charge definition for a spherical charged particle, the *electrophoretic velocity* is expressed by the so-called *Huckel equation* [*Probstein, 2003*]:

$$\mathbf{v}_{EP,\text{thick EDL}} = \frac{2}{3}\frac{\zeta\varepsilon\varepsilon_0(1+\kappa r_p)}{\mu}\mathbf{E} \approx \frac{2}{3}\left(\frac{\zeta\varepsilon\varepsilon_0}{\mu}\right)\mathbf{E}\ . \qquad (2.14)$$

If, on the other hand, we have an EDL thickness much smaller than the particle size (referred above as the thin-EDL case), then the surface of the particle can be considered as a plane *locally*. For this case, the EDL in the particle-liquid interface is identical to the EDL in the wall-liquid interface described above. Here **E** can be considered to be parallel to the particle surface, and the electrophoretic velocity is similar to the Helmholtz-Smoluchowski equation (2.11):

$$\mathbf{v}_{EP,\text{thin EDL}} = \left(\frac{\zeta\varepsilon\varepsilon_0}{\mu}\right)\mathbf{E}\ . \qquad (2.15)$$

The only difference between equations (2.15) and (2.11) is the sign. This should be expected, because electrophoresis (motion of solids relative to stationary liquids) is the complement of electro-osmosis (motion of liquids relative to stationary solids).

Besides the electrophoretic velocity, another parameter is usually used to perform comparisons between different electrophoresis experiments. This parameter, called the *electrophoretic mobility*, is defined as the ratio between **E** and $\mathbf{v}_{EP}$.

II.5 Dielectrophoresis

Dielectrophoresis is the motion of particles or molecules, relative to the surrounding liquid, caused by *polarization* effects in an applied *non-uniform* electric field [*Pohl, 1978*]. Some important differences between dielectrophoresis and electrophoresis are [*Jones, 1995*]:

- Dielectrophoresis does not require the particles to be charged.
- Dielectrophoresis occurs only when the electric field is not uniform.
- The dielectrophoretic force does not depend on the electric field polarity, and can be excited using either AC or DC electric fields.
- The dielectrophoretic force is proportional to the particle volume, while the electrophoretic force is proportional to the particle radius.

When a particle is polarized and forms a dipole, the *dielectrophoresis force* acting on the particle can be written as:

$$\mathbf{F} = \mathbf{p} \bullet \nabla\mathbf{E}\ , \qquad (2.16)$$

where **p** is the dipole moment vector. The term $\nabla\mathbf{E}$ in equation (2.16) shows that the dielectrophoretic force is a function of the *gradient* of the electric field.

For the case of a spherical *lossless* dielectric sphere immersed in a dielectric liquid, the *dielectrophoretic force* becomes [*Jones, 1995*]:

$$\mathbf{F}_{DEP} = 2\pi\varepsilon_l\varepsilon_0 r_p{}^3 \left(K\right)\nabla\mathbf{E}^2 \ , \tag{2.17}$$

$$K = \frac{\varepsilon_s - \varepsilon_l}{\varepsilon_s + 2\varepsilon_l} \ , \tag{2.18}$$

where ε_l is the liquid permittivity, K is the so-called Clausius-Mossoti (CM) function, and ε_s is the sphere permittivity. For the case of particles with electrical losses, the relative permittivities in the CM function take on complex values, with the imaginary parts corresponding to dielectric losses. Meanwhile, for the case where the particle and the liquid are conductive, the permittivities in the CM function are replaced by the conductivities of the particle and the liquid [*Jones, 1995*].

The magnitude of the CM function shows the strength of the polarization effect, while its sign determines the direction of the particle motion. If the sign of the CM function is positive, the dielectrophoretic force pulls the particle towards the regions with highest electric field gradient. This is called *positive dielectrophoresis*. If, on the other hand, the sign of the CM function is negative, then the dielectrophoretic force repels the particle away from the regions with highest electric field gradient. This is usually referred to as *negative dielectrophoresis*.

When a particle is moving dielectrophoretically inside a liquid, the *dielectrophoretic velocity* of the particle can be calculated when the motion reaches equilibrium. When this occurs, the dielectrophoretic force is equal to the Stokes drag force. For a spherical particle, the dielectrophoretic velocity then becomes:

$$\mathbf{v}_{DEP} = \frac{\mathbf{p} \bullet \nabla\mathbf{E}}{6\pi\mu r_p} \ . \tag{2.19}$$

As in the case of electrophoresis, a parameter has been defined for comparisons among different dielectrophoresis experiments. This parameter, known as the *dielectrophoretic mobility*, is defined as the ratio between $\nabla|\mathbf{E}|^2$ and $\mathbf{v}_{DEP}$.

II.6 From microfluidics to nanofluidics

There are several important differences between electrokinetic phenomena in microfluidic and nanofluidic channels. We describe them in this section.

The characteristic EDL thickness (see Equation 2.1) depends on the concentration of ions in the liquid solution inside the channels. As examples, in the case of symmetrical electrolytes (e.g.: NaCl, where z = 1), ionic concentrations of 10^{-2} M and 10^{-6} M result in κ^{-1} values of 3 nm and 300 nm, respectively. Therefore, even though the characteristic EDL thickness can be considered as thin inside microfluidic channels (where channel depths are larger than 1 μm but smaller than

1 mm), its thickness can be significant inside nanofluidic channels (where channel depths are below 1 μm).

When the characteristic EDL thickness is sufficiently thick, such that the ion concentration at the center of the nanofluidic channels is not equal to the ion concentration of the bulk liquid solution, the Boltzmann distribution (see equation 2.3), and consequently also the Poisson-Boltzmann (see equation 2.10), becomes invalid. In the case of electro-osmosis, another description for the electro-osmotic velocity may then need to be derived to replace the Helmholtz-Smoluchowski equation given in equation 2.11.

Another effect of a thick EDL is the flow profile inside the channels. In microfluidic channels, the velocity profile of electro-osmotic flow is much more uniform than in pressure-driven flow, because the EDL's diffuse layer (where the velocity gradient occurs in the electro-osmotic flow) is very thin. In nanofluidic channels, however, the characteristic EDL thickness becomes significant and the velocity gradient occurs almost everywhere in the channels, such that the electro-osmotic flow loses its uniform velocity profile [*Li, 2004*].

In section 2.4, we described electrophoresis phenomena, including the case where the EDL thickness is much larger than the particle size. A more extreme case may occur inside nanofluidic channels, where the EDL thickness is even larger than the channel depth. In this case, the charged particle may find it difficult to enter the nanofluidic channels: generally only counter-ions are allowed to enter the channels, while co-ions (including the charged particle and biological molecules, if their surface charges are like the channel walls surface charge) are repelled from the nanofluidic channels. This practical problem will become relevant for our investigation.

For dielectrophoresis, the main effect of going from microfluidics to nanofluidics is not related to the EDL thickness around channel walls and particles, but instead related to the length scale of the particles and of the features fabricated in the channels. On one hand, the dielectrophoresis effect can be reduced if we go from microfluidics to nanofluidics: the dielectrophoretic force (see equation 2.17) is proportional to the volume of the particle, which means that dielectrophoresis is much less significant on nano-scale particles than on micrometer-scale particles. On the other hand, the dielectrophoresis effect can be enhanced in the case of nanofluidics, if we can employ the nano-sized features in the nanofluidic channels to induce a high gradient of the electric field, which is the main driving force of dielectrophoresis. Therefore, a delicate relation between the sizes of particles and of the features fabricated in the channels determines the strength of dielectrophoresis in nanofluidic channels.

II.7 DNA as polyelectrolytes

DNA molecules are polymers comprising repeating units called nucleotides, which are connected to each other by a backbone formed by sugars and phosphate groups. The negative charges found in DNA molecules originate from the phosphate groups. Therefore, a DNA molecule can also be considered as a *polyelectrolyte*, where each repeating unit in the polymer behaves as an electrolyte [*Viovy, 2000*]. Consequently, a DNA molecule under an electric field also experiences electrokinetics and all the electrokinetic phenomena described in the previous sections can be applied to DNA molecules.

For most cases, a DNA molecule forms a random coil in an unconfined space [*Viovy, 2000*]. The sizes of the DNA molecules are typically expressed using their radius-of-gyration, R_g, which is defined as the square-root of the average square distance between each monomer in the DNA and the centre-of-mass of the DNA [*Rubinstein and Colby, 2003*]:

$$R_g{}^2 \equiv \frac{1}{N}\sum_{i=1}^{N}(R_i - R_{cm})^2 . \qquad (2.20)$$

A DNA molecule can be represented as a flexible cylinder with a certain diameter and contour length. In an aqueous solution, an electric double layer is also formed around each DNA molecule. The conformation of DNA (i.e. its structural arrangement) depends on the thickness of the electric double layer (characterized by κ^{-1}, see equation 2.1), relative to the polymer diameter and contour length.

If an electric field is applied on a DNA molecule, electrophoretic motion is induced on each segment of the molecule. When κ^{-1} is small compared to the molecule diameter, the electric double layer around the molecule screens hydrodynamic interactions between the molecule segments. Due to this hydrodynamic screening, the molecule does not behave as a massive coil anymore, and fluid can penetrate between the molecule segments. Consequently, the electrophoretic mobility of the DNA becomes independent of the DNA contour length: both the electrophoretic force (which propels the DNA forward) and the hydrodynamic drag force (which drag the DNA backward) are proportional to the DNA length [*Viovy, 2000*].

Note that when a DNA molecule has to enter a microfabricated nanofluidic channel, in particular where the nanofluidic channel depth is smaller than the molecule coil size, the upper and lower nanofluidic walls will confine the DNA molecule. This confinement also screens hydrodynamic interactions between the molecule segments, which produces the same results as above: the DNA electrophoretic mobility becomes independent of the molecule length, rendering electrophoretic length-based DNA separation to be generally impossible without any sieving medium.

Electrophoresis is not the only electrokinetic method that can be used to manipulate and transport DNA molecules. Electro-osmosis, which induces motion of a liquid solution around the DNA molecules, is also an important issue. Dielectrophoresis can also be applied to trap or separate DNA molecules. Chou et al. have reported dielectrophoresis of DNA molecules [*Chou et al., 2002*] where they propose the distortion of the counter-ions surrounding the DNA as the polarization mechanism driving the dielectrophoresis of DNA.

II.8 Quantitative optical imaging

Optical methods are powerful for studying both the liquid flow and the DNA motion under electrokinetics in microfabricated channels. The studied phenomena are usually imaged using an optical microscope coupled to a CCD (charged-coupled devices) camera, where the image can then be transferred to a computer for digital processing and analysis. *Fluorescence* is usually the method of choice to study properties of a liquid flow, due to the availability of bright fluorochromes, which allow for sensitive detection [*Parikesit, 2008*].

In fluorescence, a photon is used to increase the energy of a fluorochrome molecule (also known as a fluorophore or a fluorescent dye) to an excited state. The fluorescence phenomenon occurs in three steps: (1) excitation of the fluorochrome by the energy absorbed from incoming light (it occurs in 10^{-15} seconds); (2) vibrational relaxation of the fluorochrome, where the energy of the fluorochrome is lowered from the original excited state to the lowest excited state (it occurs in 10^{-12} seconds); and (3) emission of light with longer wavelength from the fluorochrome (it occurs in 10^{-9} seconds) [*Murphy, 2001*]. The shift of wavelength from the excitation light to the emission light is termed as the *Stokes shift*. Once a fluorochrome molecule reaches its original state, it can be excited again, and the fluorescence signal can be generated repeatedly using a continuous excitation light.

The fluorescence signal given by the emission light can be significantly reduced by two different phenomena: *quenching* and *photobleaching*. In quenching, the excited fluorochrome molecule loses its energy non-radiatively, for example through collisions with other molecules. Photobleaching is the irreversible destruction of the fluorochrome molecules using very intense excitation light. For imaging purposes, both quenching and photobleaching should generally be avoided. However, for quantitative visualization of transport phenomena in nanofluidics, these phenomena can be useful, as will be discussed below.

There have been many flow visualization methods being developed for macro-scale fluid flow (for example: hot-wire anemometry), but most of them are not suitable for nanofluidic measurements because they are too intrusive [*Sinton, 2004*]. Fluorescence measurements are very suitable for quantitatively visualizing flow in nanofluidics and microfluidics, because it is non-intrusive and it allows for measurements with a high spatial resolution.

Fluorescence-based flow visualization methods can be categorized into two types: particle-based methods and scalar-based methods [*Sinton, 2004*]. In particle-based methods, the fluid motion is deduced from the observed motion of fluorescence particles embedded in the fluid. The fluorescence particles are typically formed as microspheres, where fluorochrome molecules coat each sphere (see for example: the FluoSpheres from Invirogen, CA, USA). To infer the fluid flow, the motion of the fluorescence particles must be processed and analyzed. Several analysis methods are available: the most popular is the so-called Micro-PIV (micro-scale particle image velocimetry). This method analyses *patterns* of particles ensembles, and infer the fluid motion by performing correlation analysis between the recorded patterns. Micro-PIV is derived from its macro-scale counterpart, PIV. An inherent problem in this method is the low number of particles captured in each image. A proposed solution is to use the full imaging resolution capacity of the system by performing single-pixel-resolution MicroPIV [*Westerweel et al., 2004*]. Another particle-based method that can be used is PTV (particle tracking velocimetry), in which *individua*l particles are tracked and the pathlines of the individual particles are analyzed to infer the fluid flow.

In scalar-based methods, the velocity of a conserved scalar is being observed and analyzed to infer the fluid flow. The fluorescence signals themselves can be used as the scalar by preparing a fluid solution containing the fluorochrome molecules. Due to the typically short fluorescence lifetime of fluorochrome molecules, however, it is difficult to visualize the fluid motion using only fluorescence; as soon as the excitation light is terminated, no emission light is generated anymore. Several schemes can overcome this problem.

The first scheme is by inducing photobleaching on the fluorochrome molecules. Prior to the measurement, the whole fluidic channel is illuminated and all the fluorochrome molecules generate emission light. Exactly at the beginning of the actual measurement, another excitation light with a much higher intensity illuminates a certain region of the fluidic channel for a very short time. To shape this certain region, for example in a straight line across the channel width, a line-shaped aperture can be positioned before the excitation filter. This extra excitation induces photobleaching, but only to fluorochrome molecules that are located within the desired region. Hence the motion of the photobleached region can be analyzed to infer the fluid flow. The main disadvantage of this method is that it needs an extra light-source for inducing the photobleaching.

The second scheme is by using the so-called caged-fluorescence dyes. The caged-fluorescence dyes are fluorochrome molecules that have been modified chemically so that they become non-fluorescent. When a certain light (normally ultra-violet light) is exposed to the caged-fluorescent dyes, however, the chemical modification is reversed and the original fluorochrome molecules become fluorescent again. Prior to the measurement, the caged-fluorescence dyes fill the fluidic channels. Exactly when the measurement starts, the ultra-violet light illuminates a certain region of the fluidic channel (for example: in a shape of a line, as in the photobleaching method described above). Therefore only caged-fluorescence dyes located within that certain region are transformed back into the original fluorochrome molecules, and the molecules motion can be studied to deduce the fluid flow. As in the photobleaching method, this method also requires an extra light-source to perform measurements.

When we shift from microfluidics to nanofluidics, the sizes of tracer-particles are more and more reduced to the limit of a single fluorescent molecule, and consequently the distinction between the scalar-based and particle-based methods becomes obsolete [*Sinton, 2004*]. In turn, the small dimensions of the nanofluidic channels also allow for increased sensitivity in the fluorescence detection. The background signal (caused by sample impurities and scattered photons) scales linearly with the size of the detection volume, while the fluorescence signal of each single-molecule is independent of the detection volume [*Dittrich et al., 2005*].

The combination of nanofluidics and optical single-molecule detection methods is also advantageous for their high spatial resolutions. In microfluidics, where the channel depth is typically much larger than the dimensions of a single-molecule fluorochrome, confocal microscopy setup is usually required to obtain spatial resolution along the channel depth [*Zander et al., 2002*]. In nanofluidics, however, where the channel depth can be on the same order as the sizes of the single-molecule fluorochromes, the spatial resolution along the channel depth is already provided by the nanofluidic confinement and a simpler microscopy setup (e.g. wide-field epi-illumination fluorescence microscopy setup) can be employed.

Optical single-molecule detection methods are also useful for localization, identification, and counting of individual biological molecules, including DNA molecules [*Dittrich et al., 2005*]. In DNA electrophoresis, DNA molecules are usually tagged using intercalating cyanine dyes. These fluorochromes are virtually non-fluorescent in solution but form highly fluorescent complexes with DNA molecules, with more than 1000-fold fluorescence enhancement [*Rye et al., 1992*]. The fluorescence signal of the DNA-dye complexes has been shown to be insensitive to the DNA base composition (the DNA sequence), and the fluorescence intensity is linearly proportional to the DNA length, which allows for fluorescence-based sizing of the DNA molecules. When tagged with these dyes, the motion of DNA molecules under electrokinetic forces can be imaged and studied in detail [*Viovy, 2000*].

III. Quasi-2D branched U-turn nanofluidic channels

III.1 The geometry of the nanofluidic channels

We focus our study on the U-turn geometry, particularly to investigate the possibility of using the U-turn channel as separation channel in LOC-based DNA sorting and characterization. The depth of the channel is chosen to be less than 1 μm in order to ensure a high probability that there is only one DNA molecule along the channel depth (where optical detection takes place). Hence we aim to detect single DNA molecules and study them using image analysis methods. The optical detection and analysis, however, should be required only for investigating the operation of the channel, thus not for sorting the molecules. We plan to separate the molecules continuously without having to use closed-loop feedback between the optical detection and the electrical actuation.

With the nanometer-scale confinement, we can expect very strong interactions between each DNA molecule and the channel walls. These interactions may, in turn, result in novel sorting and characterization methods for single DNA molecules. On top of that, such a nanofluidic channel could also allow us to study fundamental physics phenomena. For example, inside nanometer-scale channels, the layer of counter-ions screening the fluidic channels walls can have significant thickness. The transverse ionic transport can also become non-negligible [*Pennathur et al., 2005*], and counter-intuitive sorting mechanisms may also occur [*Garcia et al., 2005*].

Figure 3.1 shows the design of our branched U-turn nanofluidic channel. The arrows in Figure 3.1.a. show the direction of liquid flow and molecule motion from the channel's inlet towards the channel's outlet. After passing a straight inlet 100 μm wide, the molecules (in solution) enter a semicircular chamber with a radius of 1 mm. It is in this chamber, that we aim to separate moving DNA molecules and sort them based on their physical characteristics (e.g. based on the length of each molecule). From the chamber, the sorted DNA molecules can exit through one of the twelve 100 μm wide sub-outlets. In this channel, the sub-outlets are then combined into a 273 μm wide outlet, but in a future version each of the sub-outlets could lead to a different chamber. At the left-upper and right-upper corners of Figure 3.1.a, two separated electrodes can be fabricated, surrounding the semicircular chamber. These embedded electrodes are not always fabricated, hence we have two versions of the channel: with and without the embedded electrodes. A photograph of the fabricated nanofluidic channel, particularly the one with embedded electrodes, is shown in Figure 3.1.b. Because the channel depth

(<1 μm) is much less than the channel lengths and widths (~100 μm), we can simplify the channel description as a quasi-two-dimensional system when we perform digital image analysis and numerical simulations.

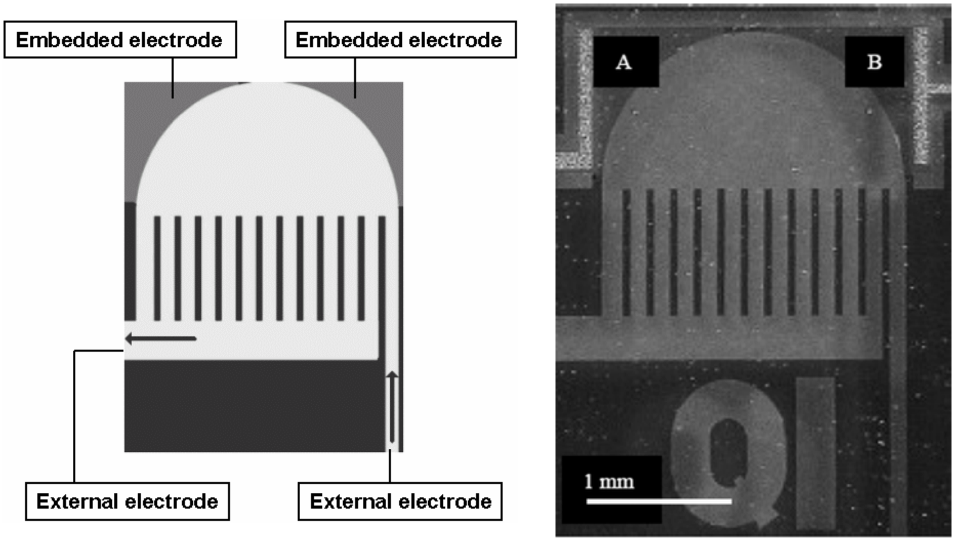

(a) (b)

Figure 3.1 The nanofluidic channel (top-view). (a) Schematic design, with the arrows showing the incoming and outgoing direction of flow. (b) A photograph of the fabricated structure. A and B show the two embedded microelectrodes, fabricated in some of the channels. The white scale bar represents 1 mm.

Various electrokinetic phenomena are potentially useful in the sorting of the molecules. These are the electro-osmosis, electrophoresis, and dielectrophoresis phenomena discussed in the previous chapter. Even without embedded electrodes (shown in Figure 3.1.b) in our nanofluidic channel, the channel's branched U-turn geometry could still be used to configure the electric fields inside the channel. However, the embedded electrodes would give a lot more freedom in our experiments: the embedded electrodes could be used as extra tools to control the electric fields. In general, by manipulating the electric fields, we intend to induce electro-osmosis, electrophoresis, dielectrophoresis, or the combinations of these to manipulate the motion of DNA molecules and to sort them. A fine control of the electrokinetic force fields [*Cohen et al., 2005*] could also be used to manipulate, control, and sort particles and molecules in the channel with a high spatial resolution.

From equations (2.9), (2.11), (2.12), and (2.19), we could see that the actual electro-osmotic, electrophoretic, and dielectrophoretic velocities throughout a nanofluidic channel depend on the electric field (**E**) distribution in the channel. Ideally, the **E** field should be calculated analytically, so that experimental electrokinetic data observed in the channel could be confirmed with an analytical solution. In our case, however, the geometry of the branched U-turn channel is too complex, such that there is no analytical solution for the **E** field. In such cases, numerical simulation of the **E** field in the studied nanofluidic channel could be used for analyzing the experimental electrokinetic data.

III.2 Fabrication of the channels-on-chips

We designed the layout of the channel, and also the structure of each mask layer in the fabrication process, using the software L-Edit (Tanner Research, Monrovia, CA, USA). In this research project, two types of microchips with embedded electrodes were fabricated to make our nanofluidic channel. The first type uses only doped a:Si (amorphous silicon) as electrodes, while the second type also employs Al (aluminium) to improve the conductance of the electrodes. Both types of microchips can be fabricated simultaneously in a single wafer, thus the fabrication method is convenient.

The embedded electrodes are self-aligned. This means the height of the electrodes and the nanofluidic channels are alike, and, in theory, no fluid leakage should occur. In the first type of microchip with embedded electrodes, the a:Si layer that is used as an electrode layer is doped with As+ (arsenic ions). These dopants are activated using excimer laser annealing with a wavelength of 309 nm. To avoid doping on unwanted regions, a protective layer comprising oxide and metal was used as a mask. This protective layer was removed afterwards. The silicon absorbs deep-UV strongly and heat is generated only in the a:Si layer. In this way, the temperature of the substrate is kept low and the glass does not soften. The fabrication starts by depositing 33 nm a:Si which is required for the bonding. As+ was implanted and activated to make the electrodes. Afterwards some undoped a:Si around the doped a:Si was removed to avoid current leakage from the doped a:Si. Finally, anodic bonding was performed where the capping wafer has pre-drilled holes for the nanofluidic channel's inlet/outlet and for access to the doped a:Si electrodes. The sheet resistance of these doped a:Si electrodes was measured as 432 Ohm/square.

To overcome the low conductance of the doped a:Si electrode, a second type of microchip with embedded electrodes was fabricated. In these chips, Al was used for the electrodes until very near the nanofluidic channels. To avoid unwanted chemical reaction between the liquid solution and a non-noble metal, Al must not directly touch the liquid solution inside the channels. Therefore, doped a:Si electrodes are used in-between the end of the Al electrodes and the nanofluidic channels. This also helps to maintain the planarity of the structure. To ensure that the bonding is properly formed, the aluminium was deposited in grooves so that their height did not exceed the nanofluidic channel's height. Fabrication began in a way similar to the first type of chips except that additional glass and a:Si layers were removed to make the groove for the Al. The As+ was also implanted and activated and some undoped a:Si around the doped a:Si was also removed. Afterwards, Al was deposited inside the groove. As the final step, anodic bonding was performed as with the first type of chip. This time, the access is to the Al electrodes, which is over the doped a:Si electrodes. To test the resistance of the electrodes, measurement of the sheet resistance was performed. The result is 0.044 Ohm/square, thus ~10,000 times more conducting than the doped a:Si electrodes.

The schematic of the fabrication steps are shown in Figure 3.2, for the first and second types of microchips with embedded electrodes. In both cases, the doped a:Si touches the edge of the nanofluidic channel. As for the microchips that are without any embedded electrodes, the fabrication steps are similar to the steps for microchips with doped a:Si electrodes, except that the As+ doping and activation are skipped [*Kutchoukov et al., 2004*].

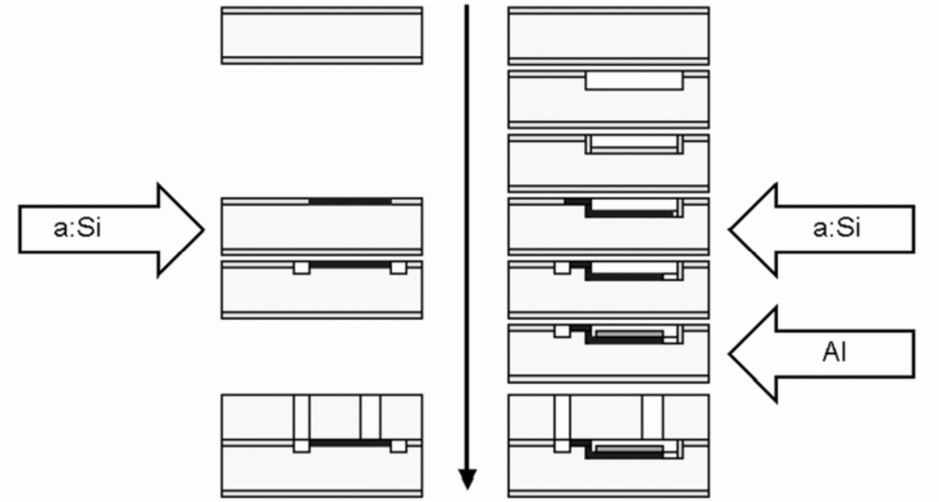

(a) (b)

Figure 3.2 Fabrication steps of the two types of microchips with embedded electrodes: (a) with only doped a:Si electrodes, and (b) including Al electrodes. The grey and black parts indicate where a:Si is doped and Al is deposited, respectively.

III.3 An interface for the channels-on-chips

Stable fluidic and electrical connections are required between the nanofluidic microchips' features (channels' inlet/outlet, embedded electrodes) and the instruments outside the microchips (fluid dispensers, fluid reservoirs, voltage sources, voltmeters, etc). To provide this, we have developed an interface for the microchips. The design of the interface is shown in Figure 3.3. The interface is fabricated from Perspex plastic (also known as *polymethyl methacrylate* or PMMA) with a dimension of 76x40x20 mm^3 (see Figure 3.4).

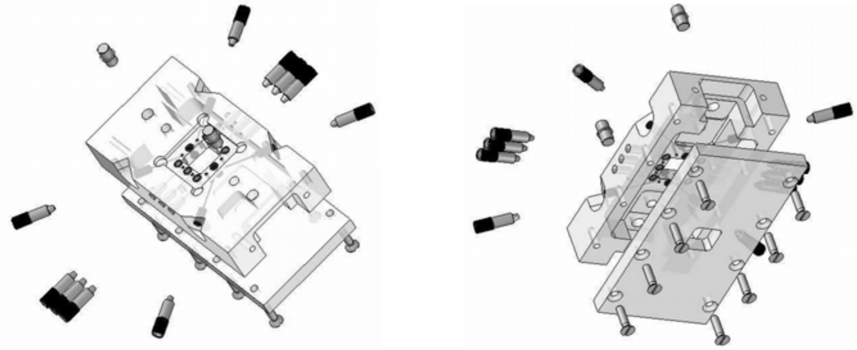

(a) (b)

Figure 3.3 Top view (a) and bottom view (b) of the interface design.

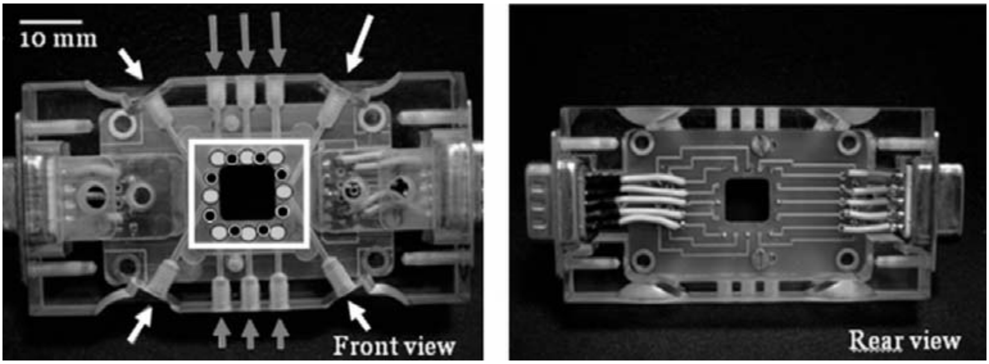

(a) (b)

Figure 3.4 Top view (a) and bottom view (b) of the fabricated interface. White square shows the chip position. The solid black circles inside the square are the positions of the electronic ports. The solid grey circles inside the square show locations where the chip is connected to the fluidic ports. The grey and white arrows show the normal and flushing fluidic ports (see text).

The interface was designed such that when the chip is held firmly in this interface, fluidic and electronic features can be controlled from external instruments with ease. The fluidic ports comprise six normal-ports (grey arrows in Figure 3.4) and two pairs of flushing-ports (the white arrows in Figure 3.4); each port can be used as an inlet or outlet. When only one end of the flushing-ports is opened, the ports act similarly to the normal-ports. When both ends of the flushing ports are opened, however, liquid solution is flushed and changed quickly from one type to another.

To connect the fluidic ports to fluid dispensers/reservoirs, commercial microfluidic parts (Upchurch Scientific, Oak Harbor, WA, USA) are used. All these fluidic ports are also equipped with gold wires for electrokinetic manipulation. For the electronic ports, Ultra-Mini Pogo Pins (Emulation Technology, Santa Clara, CA, USA) are employed. These pins ensure firm connections between the embedded electrodes in the nanofluidic microchips and the gold wires in the interface. At the bottom part of the interface, a printed-circuit-board (PCB) is attached, and it connects both the pogo-pins and fluidic ports' gold wires to external cable connections. In total, the board has eight pogo-pins (located at the solid black circles inside the square in Figure 3.4) and eight gold wires (placed at the solid grey circles inside the square in Figure 3.4), and is designed to allow voltages up to 500 Volts [*Parikesit et al., 2004*].

On the top part of the interface, a 20x20 mm^2 groove was made to hold the nanofluidic chip. A window hole was made through the center part of the interface from top to bottom, so that this versatile interface can be used with both upright and inverted microscopy setups.

III.4 Epilogue: Problems with the embedded electrodes

In the course of this project –but only after the publications of materials contained in this chapter– we discovered a persistent problem in the channels with embedded electrodes: fluidic leakages occur in these channels, mostly near the embedded electrodes. Those leakages are not controllable and not repeatable, therefore they cannot be compensated systematically. We have, therefore, focused our subsequent investigations only on the microchips without the embedded electrodes.

IV. Electro-osmotic flow analysis of a branched U-turn nanofluidic channel

In this chapter[1], we present the analysis of electro-osmotic flow in a branched U-turn nanofluidic channel, which we developed for detection and sorting of single molecules. The channel, with a depth of only 150 nm, is designed to optically detect fluorescence from a volume as small as 270 attoliters (al) with a conventional wide-field fluorescent microscope. We use distilled water as the liquid, in which we add 110 nm diameter fluorescent beads employed as tracer-particles. Quantitative imaging is used to characterize the pathlines and velocity distribution of the electro-osmotic flow in the channel. Due to the channel's complex geometry, the electro-osmotic flow cannot be solved analytically. Therefore, we use numerical flow simulations to model our channel. Our results show that the measured Brownian motion of the tracer-particles, which was not incorporated in the simulation, can explain the deviation between measured and simulated data.

IV.1 Introduction

In the last few years, a large number of microfluidic and nanofluidic channels have been studied, driven by the motivation to develop bio-medical applications that consume small amounts of reagents and analytes. Among these, one important explored direction is the development of channels that allow for single molecule detection (SMD) and single molecule manipulation (SMM) [*Foquet et al., 2004*; *Stavis et al., 2004*]. If a reliable SMD method exists, it will allow for a sensitive detection of very low concentrations of the tested fluid, a key issue in medical diagnostics. In most of the research, fluorescence is the method of choice. This is due to the availability of bright fluorochromes, well-developed optical microscopy detection methods, and large variety of bio-assays for observing biological entities.

The main challenge in SMD is to optically detect small volumes. Different methods have been described including the use of submicrometer-sized fluidic channels [*Stavis et al., 2004*]. The major challenge in SMM is the precise manipulation of single molecules which requires sufficient control of the molecule and the flow. Many lab-on-a-chip applications use electro-osmotic flow to solve this challenge. In electro-osmotic flow, an applied electric field causes the motion of ions inside the electric-double-layer (EDL) near the fluid-solid interface. Due to the viscosity of the fluid, the motion of the ions in the EDL induces the motion of the bulk fluid [*Hunter, 2001*]. The electro-osmotic flow is sometimes preferred to pressure-driven flow [*Laurell et al., 2004*; *Li, 2004*; *Nguyen and Wereley, 2002*]. The main reasons are: (1) the pressure required to drive the flow in very small fluidic channels can become impractically high; (2) it is much easier to incorporate microelectrodes than moving-micromechanics (viz. pumps and valves) in the nanofluidic chips; and (3) the electrodes needed for electro-osmotic pumping are more durable than the moving-mechanics needed for pressure-driven pumping.

---

[1] Published as: [*Parikesit et al., 2005*]

In order to perform an efficient study on single molecules, both the challenges of SMD and SMM have to be simultaneously solved. Recently we developed a nanofluidic channel, designed for detection and sorting of single molecules in solution. The lateral dimensions of the channel are on the scale of ~100 µm. Meanwhile, the fluidic channels have a depth of 150 nm, allowing us to perform fluorescence optical detection in a volume as small as 270 attoliters (al) with a conventional wide-field fluorescent microscope. The molecule-sorting scheme will rely on electrophoresis and dielectrophoresis, combined with the branched U-turn shape of the channel. Using the scheme, single molecules in the solution will be sorted based on their charge, mobility, and polarizability. Previously, we proposed a molecule-sorting nanofluidic channel [*Parikesit et al., 2004*]. The electro-osmotic flow of the channel itself, however, has yet to be analyzed. Such an analysis is required in order to characterize electro-osmotic flow in the channel.

In this chapter, we present the electro-osmotic flow analysis of the nanofluidic channel. The electro-osmotic flow inside the channel is characterized by means of quantitative imaging. The images of the tracer-particles in the fluid are captured, and the pathlines and the velocity distribution of the fluid in the channel are analyzed. We use a 20x objective lens (NA=0.4) that provides a depth-of-field of around 3 µm (in air, for light with a wavelength of 500 nm) [*Murphy, 2001*], much thicker than our 150 nm deep fluidic channels. The tracer-particles, therefore, are always in optical focus and the quantitative imaging is simplified into a “two-dimensional” particle-tracking problem.

The result of the quantitative imaging needs to be modelled. Due to the channel’s complex geometry (compared to the simple geometries commonly found in many lab-on-a-chip channels like cross sections [*Dutta et al., 2002a*; *Jin et al., 2003*; *Mitchell et al., 2000*; *Lin et al., 2002*; *Patankar et al., 1998*], straight channels, U-turns [*Dutta et al., 2002b*; *Yang et al., 2001*], and T-junctions [*Dutta et al., 2002b*; *Bianchi et al., 2000*]), it is not possible to build an analytical model. We perform, therefore, numerical flow simulations to model the flow in the channel.

In performing a numerical flow simulation on a channel with such a complex geometry, we also take advantage of the dimensions of the channel. Because the 150 nm channel depth is much smaller than the ~100 µm lateral dimensions of the channel, the flow geometry is compatible with that of Hele-Shaw flow [*Faber, 1995*]. This implies that the steady flow pattern averaged over the channel depth can be described in terms of two-dimensional potential flow (which is independent of fluid viscosity). This considerably simplifies the flow analysis into a two-dimensional-like problem. The simulation does not incorporate Brownian motion, which can be significant during the measurement. We will discuss the consequences of this later.

The microphotograph of our nanofluidic channel is shown in Figure 4.1. The 150 nm channel depth allows us to detect a volume as small as 270 attoliters (al), a value that is adequate for sensitive SMD [*Zander et al., 2002*]. The arrows indicate the flow direction. The solution of single molecules pass through a 100 μm -wide straight channel, before entering a semi-circular chamber with a radius of 1 mm. Twelve 100 μm wide sub-outlets collect the fluid out of the chamber (depending on the flow pattern) into a 273 μm wide main outlet. Applying positive and negative voltages to the inlet and the outlet, respectively, induces electro-osmotic flow. Four similar channels are manufactured on a 20x20 mm^2 chip as shown (top-view) in Figure 4.1. Grey parts indicate the fluidic channels.

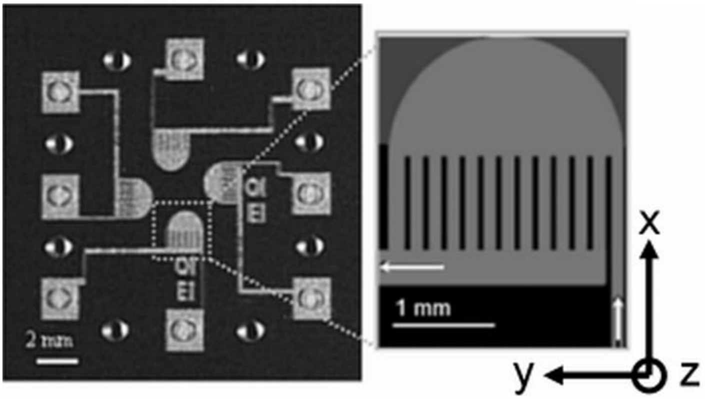

Figure 4.1 A microphotograph of the channels-on-chip; the zoomed-in part is the scheme for each channel, with the arrows indicating the flow direction. A Cartesian coordinate system, used in the analysis, is also shown.

A channel with a similar (but not curved) geometry has been analyzed experimentally [*Takamura et al., 2003*] and theoretically [*Brask et al., 2002*]. The electro-osmotic flow in that channel, however, is induced primarily by the built-in electrodes whereas the electro-osmotic flow in our channel is only driven by external electrodes. The configuration of the electro-osmotic pumping, therefore, is significantly different between the two channels. Their channel is designed for efficient low-voltage electro-osmotic pumping while our channel is designed for particle detection and sorting.

IV.2 Analysis methods

The electro-osmotic flow analysis is first studied by performing quantitative imaging. In order to model and analyze the experimental results, however, we also perform a numerical flow simulation on the channel. The thin fluidic channel depth (150 nm) serves two advantages for the quantitative imaging: (1) the channel is always at the center of the optical depth-of-field, and (2) all tracer-particle are always in optical focus. Hence, the quantitative imaging is simplified into two-dimensional particle tracking. Moreover, the very thin fluidic channel depth is also advantageous for the numerical flow simulation. Modelling can be performed in two dimensions, reducing computational cost and complexity.

We start by describing the governing equations and proceed with explaining the quantitative imaging and numerical flow simulation methods used for the analysis.

IV.2.1 Governing equations

In chapter 2, we have described the fundamentals of electrokinetics in microfabricated channels. The governing equations of the liquid flow are the continuity equation and the momentum equation:

$$\nabla.\mathbf{v} = 0 \text{ and } \rho\left(\frac{\partial v}{\partial t} + (\mathbf{v}.\nabla)\mathbf{v}\right) = -\nabla P + \mu\nabla^2\mathbf{v} + \rho_e\mathbf{E}\,, \quad (4.1)$$

while the governing equation for the electric potential distribution in the channels is the Poisson equation:

$$\nabla^2\psi = -\frac{\rho_e}{\varepsilon\varepsilon_0}\,. \quad (4.2)$$

An important parameter in analyzing the electro-osmotic flow in nanochannels is the ‘characteristic EDL thickness’:

$$\frac{1}{\kappa} = \sqrt{\frac{\varepsilon\varepsilon_0 k_b T}{2Z^2e^2n_\infty}}\,. \quad (4.3)$$

The fluid in our experiments is distilled water, for which the 'characteristic EDL thickness' is on the order of 1 µm. This is much larger than the channel depth and hence EDL overlap occurs. Verwey and Overbeek [*Verwey and Overbeek, 1948*] were the first to develop a theoretical model for the potential distribution in case of overlapping EDLs, based on the Poisson-Boltzmann equation. This equation uses the Boltzmann distribution of the ionic number concentration, and hence assumes an infinitely large liquid medium. This means that using this model for overlapping EDLs is questionable. Other researchers [*Conlisk et al., 2002*; *Qu et al., 2000*] have tried to solve this inconsistency and have proposed a more elaborate model for overlapping EDLs. It was shown [*Qu et al., 2000*] that especially in the case where the 'characteristic EDL thickness' is comparable to the channel depth, substantial deviations from the theory of Verwey and Overbeek and their model occur. By comparing the results of others [*Conlisk et al., 2002*; *Qu et al., 2000*; *Yao et al., 2003*], however, it can be concluded that the results of the more elaborate models all converge to the result of the model of Verwey and Overbeek in the case of a very thick EDL (as in the present case). This implies that in our case the Poisson-Boltzmann equation should be applicable:

$$\nabla^2\psi^* = \kappa^2 \sinh\left(\psi^*\right), \tag{4.4}$$

where Ψ^* is the reduced potential defined as $\Psi^*=(Ze\Psi)/(k_bT)$.

According to Yao et al. [*Yao et al., 2003*], when the 'characteristic EDL thickness' is in the order of, or higher than, 10 times the channel depth (as in the present case), no substantial deviations occur in the results of the non-linear and linear Poisson-Boltzmann equation. In the present case, therefore, the Debye-Huckel linearization approximation $Ze\Psi << k_bT$ on the Poisson-Boltzmann equation can be used and the Poisson-Boltzmann equation can be expressed as:

$$\nabla^2\psi^* = \kappa^2\psi^*, \tag{4.5}$$

and the Poisson equation can be re-written as:

$$\rho_e = -\varepsilon\varepsilon_0\kappa^2\psi . \tag{4.6}$$

Because of the very large value of the 'characteristic EDL thickness', we can assume that the electric potential in the liquid, Ψ, is everywhere equal to ζ, the electric potential in the electric double-layer. Hence the local net charge density can also be assumed constant everywhere in the liquid as:

$$\rho_e = -\varepsilon\varepsilon_0\kappa^2\zeta . \tag{4.7}$$

Both the classical theory and the more elaborate theories of Conlisk et al. and Qu et al. predict this [*Conlisk et al., 2002*; *Qu et al., 2000*].

Inside micro/nano-fluidic channels, the flow is typically steady and has a low Reynolds number (in our channel, the Reynolds number is on the order of 10^{-3}). Therefore when there is no applied pressure gradient, the momentum equation can be written as:

$$0 = \mu\nabla^2\mathbf{v} - \varepsilon\varepsilon_0\kappa^2\zeta\mathbf{E} . \tag{4.8}$$

We employ a Cartesian coordinate system (shown in Figure 4.1), in which the z-axis represents the axial dimension (i.e. the channel depth) while the x- and y-axis correspond to the lateral dimensions (i.e. the channel widths and lengths, respectively). Due to the dimensions of our nanofluidic channel, the role of the EDL is much greater in the z-direction than in the other directions. On the other hand, because the channel depth is constant everywhere, the z-component of **E** is zero. Meanwhile, the channel depth is also much smaller than the length and the width of channel. Hence $\partial^2\mathbf{v}/\partial z^2 >> \partial^2\mathbf{v}/\partial x^2, \partial^2\mathbf{v}/\partial y^2$. The momentum equation can then be approximated as:

$$\frac{\partial^2\mathbf{v}}{\partial z^2} \approx \frac{\varepsilon\varepsilon_0\kappa^2\zeta}{\mu}\mathbf{E}(x,y) . \tag{4.9}$$

Using the boundary conditions $\mathbf{v}|_{z=\pm h/2}=0$ and $\partial\mathbf{v}/\partial z|_{z=0}=0$, where h is the channel depth, the solution for the electro-osmotic velocity, **v**, is (for a constant charge density):

$$\mathbf{v_{EO}}=\frac{\varepsilon\varepsilon_0\kappa^2\zeta}{2\mu}\mathbf{E}\left(z^2-\frac{h^2}{4}\right), \qquad (4.10)$$

which is similar to a Poiseuille velocity profile between two infinite plates separated by a distance h. If ζ is negative (i.e. for negatively charged channel walls), the counter-ions in the EDL are positive and the electro-osmotic flow is towards the negative electrode [*Li, 2004*]. The average value of **v** in z-direction can be expressed as:

$$\mathbf{v_{EO,average}}=\frac{1}{h}\int_{-h/2}^{h/2}\mathbf{v_{EO}}dz=\frac{-\varepsilon\varepsilon_0\zeta}{\mu}\frac{\kappa^2h^2}{12}\mathbf{E}. \qquad (4.11)$$

This approach is similar to the Hele-Shaw approximation [*Faber, 1995*], named after Hele-Shaw (1898). The velocity field at a certain constant z (or averaged with respect to z) is only a function of the (x,y) plane. The parabolic velocity profile can be physically explained by the constant value of Ψ caused by the very large 'characteristic EDL thickness'. The electric field induced by the electrodes at the ends of the channel drive every part of the liquid in the channel. The velocity decreases as we go near the channel walls, because of the no-slip condition there. A theoretical study on various electro-osmotic velocity profiles as a function of EDL thickness, which gives the parabolic velocity profile that we get, has been done before [*Burgreen et al., 1964*; *Rice et al., 1965*].

In our measurements, we use beads with a diameter of 110 nm inside channels with a depth of 150 nm. Because the diameter of the beads is almost as large as the channel depth, the electro-osmotic velocity experienced by the beads will have a value between $\mathbf{v}_{\mathrm{EO,average}}$ and $(3/2)\mathbf{v}_{\mathrm{EO,average}}$ (i.e. between the 'averaged velocity' and the 'maximum velocity' in the parabolic velocity profile). Hence the effective electro-osmotic velocity of the beads is not exactly as the value expressed in (4.11). A correction factor, C_1, is needed to compensate the exact Hele-Shaw approach used in (4.11): $\mathbf{v}_{\mathrm{EO,beads}} = C_1\,\mathbf{v}_{\mathrm{EO,average}}$.

Meanwhile, the interface between the beads and the distilled water will induce another EDL, with a different electric potential, ζ_p. Because of this EDL, the spherical beads experience an electrophoretic motion with a velocity of [*Nguyen et al., 2002*]:

$$\mathbf{v_{EP,beads}}=\frac{\varepsilon\varepsilon_0\zeta_p}{\mu}\mathbf{E}. \qquad (4.12)$$

The direction of the electrophoretic motion of the beads is opposite to the direction of the electro-osmotic liquid motion. When we characterize the electro-osmotic flow in the channel using the beads, we have to take into account this electrophoretic motion of the beads. The apparent electro-osmotic velocity observed in the experiment will therefore be:

$$\mathbf{v} = \mathbf{v}_{\mathbf{EO,beads}} + \mathbf{v}_{\mathbf{EP,beads}} = \frac{\varepsilon\varepsilon_0}{\mu}\left(\frac{-\kappa^2\zeta h^2}{12}C_1 + \zeta_p\right)\mathbf{E}. \quad (4.13)$$

When compared to the commonly-used Helmholtz-Smoluchowski equation [*Li, 2004*] (which is only valid for a thin EDL layer)

$$\mathbf{v}_{\mathbf{Helmholtz\text{-}Smoluchowski}} = \frac{-\varepsilon\varepsilon_0\zeta}{\mu}\mathbf{E}, \quad (4.14)$$

the apparent electro-osmotic velocity in (4.13) can be written as:

$$\mathbf{v} = \frac{-\varepsilon\varepsilon_0\zeta_{EFF}}{\mu}\mathbf{E}, \quad (4.15)$$

with ζ_{EFF} as an effective zeta potential. This parameter ζ_{EFF} merges ζ (the original zeta potential used in Helmholtz-Smoluchowski equation) with C_1 (the correction factor that compensates for the difference between the Hele-Shaw approximation result and the real electro-osmotic velocity experienced by the beads) and ζ_p (the zeta potential between the beads and the water, which induces the electrophoretic motion of the beads).

In (4.15), the local velocity is still directly related to the local electric field strength inside the channel. The equation also has the same format as the Helmholtz-Smoluchowski equation, except that the zeta potential is now replaced by an effective zeta potential. As can also be seen from the equation, because there is no applied pressure gradients, the local velocity everywhere in the fluid is linearly proportional to the local electric field strength; this is called the similarity between velocity and electric field [*Cummings et al., 2000*; *Santiago, 2001*].

In the experiments, only the apparent electro-osmotic velocity, v, can be measured directly. In the numerical simulation, only the local electric field strength, **E**, is simulated. The effective zeta potential, ζ_{EFF}, is then employed in the simulation to calculate the electro-osmotic velocity, **v**.

IV.2.2 Quantitative Imaging

To perform quantitative imaging on the electro-osmotic flow in our complex geometry nanofluidic channel, we use fluorescent beads as the tracer-particles. The 110 nm -diameter beads are carboxylated-modified FluoSpheres from Molecular Probes (Eugene, OR, USA). The beads' excitation and emission peaks are 580 nm and 605 nm, respectively. The beads are diluted in distilled water with a 1:1000 volume ratio.

A drop of the solution is pipetted into the channel's fluidic inlet, and capillary forces pull the fluid into the channel. The channel-on-chip is then clamped in the chip's interface, before the interface's inlet and outlet are filled with the same solution. For applying electro-osmotic voltage differences, outputs from an E303-3 Delta Elektronika (Zierikzee, The Netherlands) voltage source is connected to the interface's respective electronic ports. If we also need to apply pressure-driven flow to the nanofluidic channel, then any of the fluidic ports can be connected via PEEK (poly-ether-ether-ketone) tubes from Upchurch (Oak Harbor, WA, USA) to a syringe, which in turn is connected to an 1215-UltraSaver EFD (East Providence, RI, USA) fluid dispenser.

Imaging is performed on a TCS SP2 Leica Mycrosystems (Wetzlar, Germany) fluorescence microscope. We use a 20x objective lens (NA=0.4) that provides a depth-of-field of ~ 3 µm, much thicker than our 150 nm channel depth [*Murphy, 2003*]. We use an N21 optical filter-set from Leica (Wetzlar, Germany) with excitation band-pass filter at 515-560 nm, dichromatic mirror at 580 nm, and suppression long-pass filter at 590 nm. The fluorescence signal is measured using an Orca-ER Hamamatsu (Hamamatsu City, Japan) CCD camera (pixel size of 6.45 µm). Binning is occasionally used to improve the signal-to-noise ratio. After examining CCD's exposure time of 50, 100, and 200 ms, we found out that 100 ms was long enough to provide a good contrast but also short enough to capture the locations of the tracer-particles without blur motion.

Image analysis is done using Matlab (Natick, MA, USA) and our image processing toolbox DIPimage [*Luengo et al., 1999*]. Static objects in the image sequence are removed by subtracting two consecutive images. To reduce computation time, the analysis is only done in a region-of-interest (ROI), which is defined as a rectangle around the tracer-particle in interest. The tracer-particles are distinguished from the background using a fixed-threshold algorithm in DIPimage [*Young et al., 1998*]. The position of the particle is then determined by measuring the center-of-gravity across the ROI. In order to track the moving particle, the ROI is also moved along the particle. The measured particle's center-of-gravity is then used to specify the center of the moved ROI. By tracking the particles through the whole image sequence, the pathlines can be determined. The velocity of a tracer-particle is calculated from the particle's distance in each pair of consecutive images and the time difference between the measured images. The precision of the center-of-gravity measurement is evaluated by doing measurements on a sequence of 200 images of static tracer-particles, resulting in standard deviations of 0.0096 µm and 0.0121 µm in x and y axis, respectively.

IV.2.3 Numerical flow simulation

It has already been established from the derivation of the governing equations that due to the dimensions of our channel, the Hele-Shaw approximation can be used. Therefore the electro-osmotic flow in our complex geometry nanofluidic channel can be obtained in a two-dimensional numerical flow simulation (along the lateral dimensions), an important advantage for the simulation.

If pressure-driven flow happens to exist in the channel, its vertically-averaged velocity distribution can also be simplified to two dimensions (i.e. only the lateral dimensions) [*Faber, 1995*]. Therefore, a two-dimensional numerical flow simulation can always be performed, even if pressure-driven flow co-exists with electro-osmotic flow in the channel. The numerical flow simulation has been carried out in a commercial flow simulation code FLUENT (Lebanon, NH, USA). According to equation 4.15, only the electric field needs to be determined. The computations of the electric field inside the channel, and the resulting electro-osmotic force, have been incorporated in a user-defined function (UDF). Using FLUENT, we calculate the pathlines and the velocities, **v**(x,y), directly from equation 4.15.

A full three-dimensional simulation of our channel, which has been validated using experimental results in more cross-channel geometries [*Markesteijn et al., 2006*], is also carried out. This is also done with UDFs, and is accomplished by solving equation 4.6 together with the momentum equations, which are coupled with each other through the electric source term. The full three-dimensional simulation gives the same results like our two-dimensional approach. This validates our two-dimensional simulation method.

IV.3 Results and discussion

The low Reynolds number in our channel implies that the inertial effects in the electro-osmotic flow are negligible, so that pathlines can make sharp corners. Figure 4.2 shows the simulation result of the pathlines (shown in grey lines) and normalized velocity values (represented by the colorbar) in the channel. Meanwhile, Figures 4.3 shows the measured pathlines (shown in white streaks), where sharp corners shows that inertial effects are negligible. These results show the velocity distribution in the channel. As predicted by equation 4.15, the local electro-osmotic velocity is proportional to the local electric-field-strength in the lateral dimensions, which in turn depends on the channel's complex geometry. The zoomed-in figure in Figure 4.2 shows a specific region in the channel. This region is interesting to analyze for two reasons: (1) due to the channel's geometry, this region has the highest velocity variation; (2) this region is where the earlier-proposed molecule sorting method [*Parikesit et al., 2004*] starts to take effect.

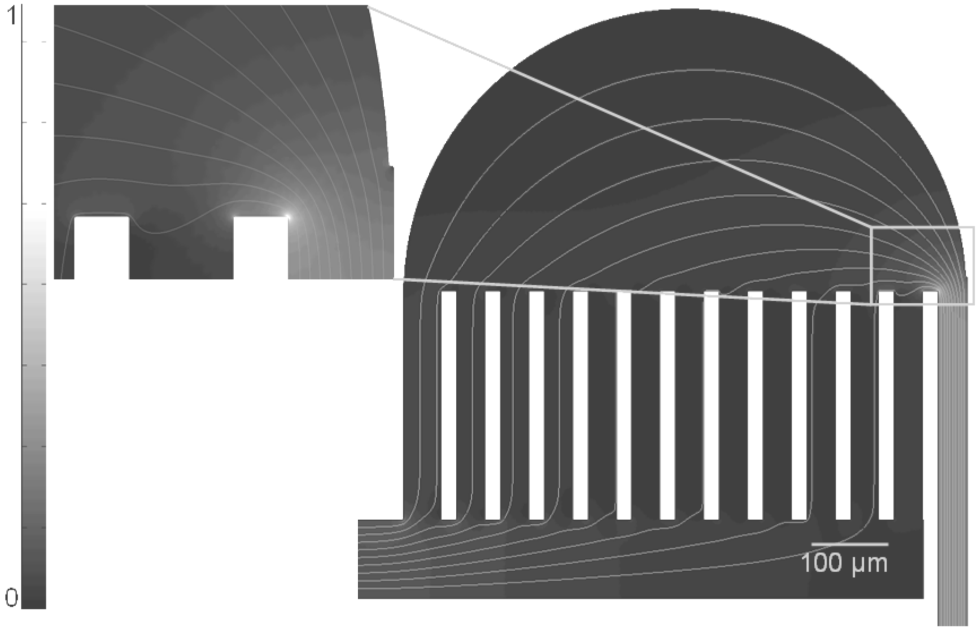

Figure 4.2 Simulation result for the pathlines (shown by the grey lines) and normalized-velocity values (represented by the colorbar) in the channel. The zoomed-in picture shows the region with the highest velocity gradient. The scale bar represents 100 µm.

In practice, deviation from the smooth low-Reynolds-number pathlines is expected due to Brownian motion of the tracer-particles. The Brownian diffusion coefficient for a spherical particle, and the corresponding mean Brownian displacement (in a two-dimension space), are:

$$D = \frac{k_b T}{6\pi\mu a}, \tag{4.16}$$

$$d = \sqrt{4Dt}, \tag{4.17}$$

where *t* is the diffusion time [*Mazo, 2002*]. Assuming a fluid dynamic viscosity, μ, of 0.001 kg/(m.s) for water, for our 20°C experimental setup we expect the Brownian diffusion coefficient of $1.95\text{x}10^{-12}$ m^2/s. This corresponds to a mean Brownian displacement of 2.79 μm, for a diffusion time *t* of 1 second. The corresponding velocity due to the Brownian motion (or as we call it, the Brownian-related-velocity) is then proportional to $t^{1/2}$.

Figure 4.3 shows both the simulated (in white lines) and the measured (in white streaks) tracer-particles' pathlines, particularly in the region depicted by the zoomed-in part in Figure 4.2. The data in Figure 4.3 (a) and (b) are for a ΔV_{EO} (applied external electric potential between the inlet and the outlet) of 100 V and 200 V, respectively. In general, the measured and simulated pathlines agree with each other. The observed deviations are caused by Brownian motion, and they decrease as ΔV_{EO} is increased. Higher ΔV_{EO} implies a higher velocity of the tracer-particles. When the velocity is significantly higher than the Brownian motion, the drift of the particles from their respective pathlines is negligible and the measured pathlines agree more closely with the simulation.

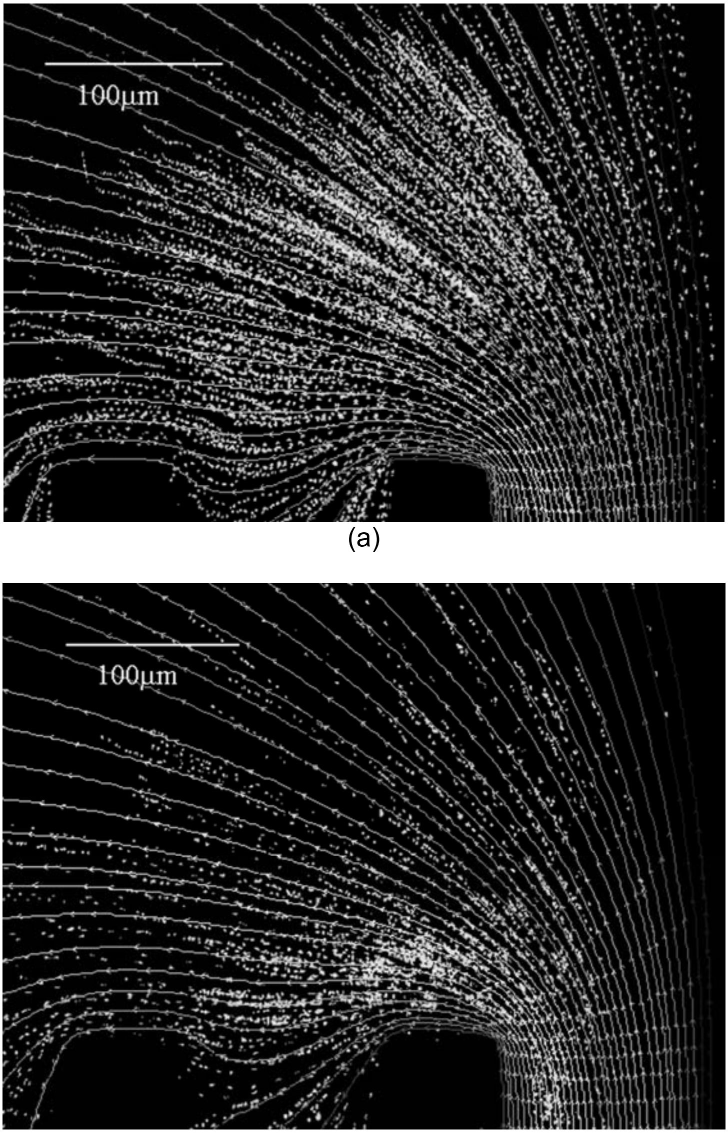

(a)

(b)

Figure 4.3 Measured (in white streaks) and simulated pathlines (in white lines) of tracer-particles, measured in the region depicted by the zoomed-in part in Figure 4.2, with ΔV_{EO} of (a) 100 V, and (b) 200 V. Both scale bars represent 100 μm.

Figure 4.4 (a) and (b) shows the analyzed velocity, for the region defined by the zoomed-in part in Figure 4.2, when we applied a ΔV_{EO} of 30 V and 50 V, respectively.

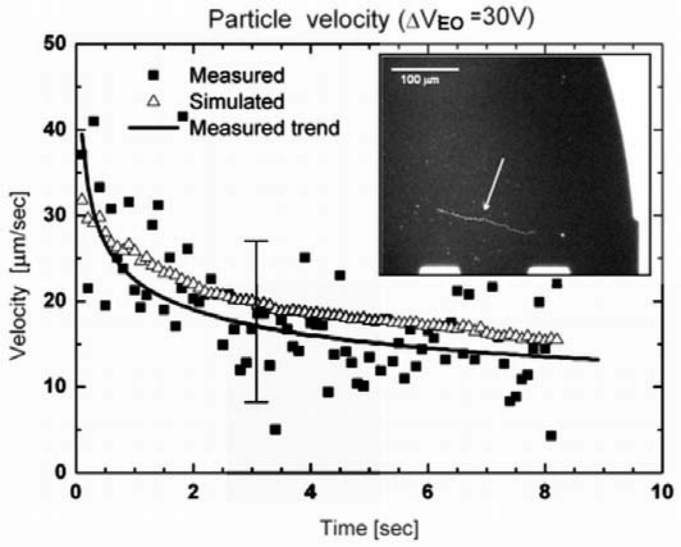

(a)

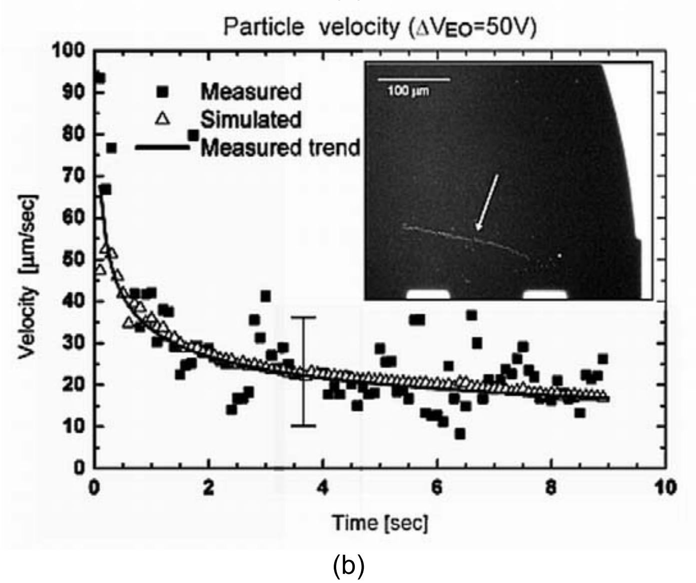

(b)

Figure 4.4 The velocity of the particles, whose pathlines are shown in the insert (with scale bars of 100 μm), when we applied a ΔV_{EO} of (a) 30 V and (b) 50 V, respectively. Measured and simulated data are shown in black squares and triangles, respectively. The measured trends (black lines) are only a visualization aid. The error bars illustrate the 95% error margin due to Brownian motion.

The insert figures in Figure 4.4 (a) and (b) shows the measured pathlines. The two particles start their pathlines from approximately the same location. In Figure 4.4, the measured and simulated velocity data are shown as the black squares and triangles, respectively. Due to the complex geometry of our channel, the data is not expected to follow any specific law. Power-law curves, shown as the black fitting-trend lines, are used only as visualization aids on the measured data. A few points in the measured data that are clearly out of the trend were omitted.

Due to the Brownian motion, the measured pathlines are not exactly the same as the simulated pathlines. In obtaining the simulated data, we use the simulated velocity values assigned on the tracer-particles' position measured in the experiment. Hence the simulated velocity values shown in Figure 4.4 are not necessarily obtained from a single simulated pathline. This makes the simulated data in Figure 4.4 appear to fluctuate.

Because the raw simulation result is only the normalized velocity, the simulated data must be scaled linearly to fit the measured data. This is done by calculating the fitting-scale that gives the minimum value of $\mathbf{v}_{\mathrm{D}}$ (i.e. velocity deviation), an "rms" parameter that we define to measure how far the measurement and the simulation deviate from each other:

$$\mathbf{v_D} = \sqrt{\frac{\sum_{n} (\mathbf{v_M} - \mathbf{v_S})^2}{n}} \ . \qquad (4.18)$$

where n is the number of images in the measured sequence, and $\mathbf{v}_{\mathrm{M}}$ and $\mathbf{v}_{\mathrm{S}}$ are the measured and simulated velocity of the tracer-particle, respectively. Only when the measured and simulated velocity data exactly match each other, is the value of $\mathbf{v}_{\mathrm{D}}$ equal to 0.

The $\mathbf{v}_{\mathrm{D}}$ values are shown in Table 4.1 for the data in Figure 4.4. We expect to always have $\mathbf{v}_{\mathrm{D}} > 0$, because of the Brownian motion of the tracer-particles (see Figure 4.3). The imaging system's frame-rates were 10 frame/sec. This means that we have the diffusion times between consecutive images of 0.1 seconds. Referring to equations 4.16 and 4.17, we expect a measured Brownian-related-velocity of 8.83 μm/s. The v_{D} values in Table 4.1 are on the same order as the expected 8.83 μm/s Brownian-related-velocity values. Therefore it is shown that the $\mathbf{v}_{\mathrm{D}}$ values can be explained by the Brownian motion of the tracer-particles, which is not incorporated in the simulation.

Table 4.1. The velocity analysis of the graphs shown in Figure 4(a) and 4(b). The expected Brownian-related-velocity value is 8.83 μm/s.

ΔV_{EO} (volts)	$\mathbf{v}_{\mathrm{D}}$ (μm/s)	Mean of $\mathbf{v}_{\mathrm{M}}$ (μm/s)
30 V	5.58	31.20
50 V	8.17	40.60

IV.4 Conclusions

Recently we developed a nanofluidic channel, designed for detection and sorting of single molecules in solution. Due to the 150 nm channel depth, fluorescence from a volume as small as 270 attoliters (al) can be detected optically with a conventional wide-field fluorescent microscope, thus allowing us to perform a sensitive SMD. The molecule-sorting scheme will rely on electrophoresis and dielectrophoresis, combined with the branched u-turn shape of the channel.

We have analyzed the electro-osmotic flow in the nanofluidic channel. Such an analysis is required in order to characterize the electro-osmotic flow in the channel prior to molecule sorting. Using quantitative imaging, we have studied the pathlines and velocity distribution in the channel. To model and analyze our experimental data, we have employed a numerical flow simulation. Such a method is necessary because the channel's complex geometry prevents us to use an analytical solution.

The two-dimensional characteristic of our channel is advantageous for quantitative imaging and numerical flow simulation because the analysis can be simplified. From the results and discussion above, two concluding points can be made. First, the electro-osmotic flow inside the nanofluidic channel has been characterized using quantitative imaging. The pathlines make sharp corners and resemble a low-Reynolds-number flow, and the velocity distribution is shown in Figure 4.2. Second, the obtained experimental data have been analyzed using modelled data from numerical flow simulation. The deviations between them are due to the Brownian motion of the tracer-particles.

Considering the significant Brownian motion effect for small molecules, the proposed molecule sorting scheme in the nanofluidic channel [*Parikesit et al., 2004*] will have to be optimized to overcome the Brownian motion. Besides that, from the governing equations it is clear that adding salt into the fluid will give some advantages: (1) the 'characteristic EDL thickness' can be reduced, so that (negatively charged) DNA molecules can enter the channels more easily; (2) the electro-osmotic velocity can be increased, and consequently the Brownian effect can be reduced.

V. Size-dependent electrokinetic pathlines of DNA molecules in sieve-less U-turn nanochannels

We demonstrate in this chapter[2], for the first time, that sieve-less U-turn nanochannels can induce size-dependent electrokinetic pathlines of DNA molecules. We experimentally use λ (48.5 kbp) and T4GT7 (165.6 kbp) DNA molecules flowing continuously inside our 400-nm-deep nanochannels. Numerical simulations indicate that the observed pathlines can be explained by dielectrophoresis, which occurs even under DC electrical fields. Our results indicate that U-turn nanochannels allow size-based DNA separation to be operated in a sieve-less and continuous manner, hence importantly enabling us to avoid complicated sieve designs while obtaining high-throughput in Lab-on-aChip systems.

V.1 Introduction

Nanofluidic channels and Lab-on-a-Chip devices have been used and developed to perform investigation on DNA molecules, an interesting issue in genomic studies and polymer science [*Tegenfeldt et al., 2004*]. The information obtained from the DNA sequence is particularly important in genomic applications, as was highlighted in the Human Genome Project [*Venter et al., 2001*]. A crucial step in the sequencing process is the size-based separation of DNA fragments under an electric field, which conventionally requires a sieving tool due to the size-independent electrophoretic DNA mobility in free-solution [*Viovy, 2000*]. In practice, the sieving tool can be in the form of a drag-tag [*Meagher et al., 2005*], gel matrices [*Viovy, 2000*], dielectrophoretic traps [*Petersen et al., 2007*; *Regtmeier et al., 2007*], membranes [*Striemer et al., 2007*], or microfabricated periodic structures [*Bakajin et al., 2001*; *Cabodi et al., 2002*; *Chou et al., 1999*; *Fu et al., 2006*; *Fu et al., 2007*; *Han et al., 2000*; *Huang et al., 2002*; *Huang et al., 2004*].

The idea of a DNA separation in Lab-on-a-Chip that does not require any sieving tool is very appealing, because extra preparatory steps (as in the cases of drag-tag and gel matrices) or complicated sieve designs (as in the cases of dielectrophoretic traps, membranes, and periodic microstructures) could then be avoided. On top of that, the DNA separation scheme should be able to run continuously, which would allow high throughput [*Eijkel et al., 2006a*]. Some interesting observations have been reported on electrokinetic phenomena of DNA in nanofluidic channels [*Baldessari et al., 2006*; *Krishnan et al., 2007*; *Riehn et al., 2006*], and very recently sieve-less DNA separation in nanochannels have been reported, although they are operated in a non-continuous manner [*Cross et al., 2007*; *Pennathur et al., 2007*]. Hence, no previous author has reported a continuous, sieve-less, DNA separation scheme inside microfabricated channels.

---

[2] Submitted as: [*Parikesit et al., 2007b*]

In this chapter, we study the electrokinetic pathlines of DNA molecules in U-turn nanofluidic channels, in order to develop a continuous, sieve-less, size-based DNA separation. We particularly investigate whether the pathlines of the molecules depends on the DNA size and the type of applied electric field. We use numerical simulation to model the influence of electro-osmosis, electrophoresis, and dielectrophoresis on the observed experimental pathlines. Furthermore, we will show how both our experimental and simulation observations indicate that, for the first time, continuous and sieve-less size-based separation of DNA molecules in Lab-on-a-Chip devices is possible.

V.2 Methods

The microphotograph and schematic view of our nanofluidic channel is shown in Figure 5.1, where the white arrows indicate the general direction of the DNA motion and the light gray parts indicate the nanofluidic channels. The solution of DNA molecules passes through a 100 μm -wide straight “inlet channel”, before entering a “semi-circular chamber” with a radius of 1 mm. Twelve 100 μm wide “sub-outlet channels” collect the fluid out of the chamber into a 273 μm wide main outlet. Negative and positive voltages are applied to the inlet and the outlet ports, respectively, in order to induce electrophoretic motion of the DNA molecules. Our nanofluidic channels have a channel depth of 400 nm and were fabricated in our own facilities using glass-to-glass anodic bonding [*Kutchoukov et al., 2004*]. Two types of dsDNA (double-stranded DNA) molecules are employed in our experiments: λ-DNA (contour length = 48.5 kbp; purchased from Promega, Madison, WI, USA) and T4GT7-DNA (contour length = 165.6 kbp; purchased from Wako Nippon Gene, Osaka, Japan). In an unconfined solution, the radius-of-gyration of the λ-DNA and the T4GT7-DNA are 0.74 μm and 1.37 μm, respectively [*Chan et al., 2006*]. Because the molecules’ radius-of-gyrations are larger than the nanofluidic channel depths, the molecules are confined and squeezed by the upper and lower walls inside the channels.

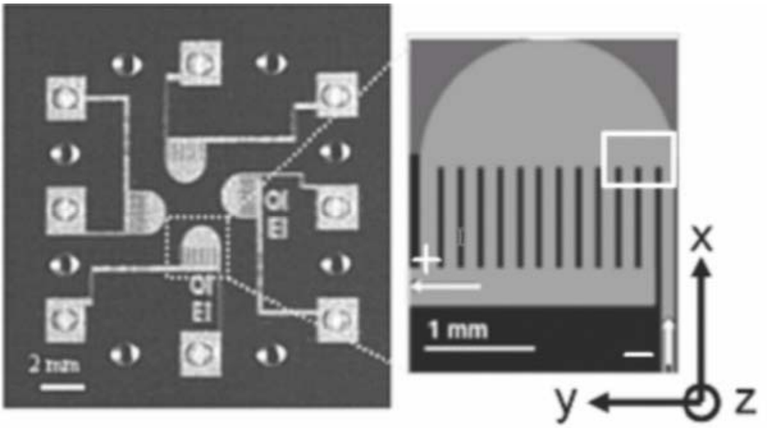

(a) (b)

Figure 5.1. (a) A microphotograph and (b) a schematic view of the nanofluidic channels, with the arrows indicating the flow direction and the rectangle showing the region of observation. A Cartesian coordinate system, used in the analysis, is also shown.

All of the DNA molecule were stained with a 1:8 (dye:basepair) ratio using a YOYO-1 dye (Invitrogen, Carlsbad, CA, USA), which has an excitation peak and an emission peak at 491 nm and 509 nm, respectively. All DNA-dye solutions were diluted with Milli-Q purified water (Millipore, Billerica, MA, USA) and then 2% (v/v) 2-mercaptoethanol was added to suppress photobleaching. The motion of individual DNA molecules inside nanofluidic channels was driven using various electric fields generated by a voltage source (Wavetek 143, Willtek, Ismaning, Germany) and then observed with a "TCS SP2 – DM RXA" Leica Microsystems (Wetzlar, Germany) microscope. We used a 20x objective lens (NA=0.4), which provides a depth-of-field of ~ 3 μm, and use an N21 optical filter-set from Leica (Wetzlar, Germany) with a Xenon lamp. The fluorescence signal was measured using an Orca-ER Hamamatsu (Hamamatsu City, Japan) CCD camera (pixel size of 6.45 μm), with an exposure time of 100 ms and a 4x4-pixels binning. The microscope is used in wide-field mode as opposed to confocal mode.

Previously (see Chapter 4) we have analyzed the electro-osmotic flow inside the branched U-turn nanofluidic channels and found that the highest electric field gradient, which could enable changes on the pathlines of the DNA molecules through dielectrophoretic effects, is located where the "inlet channel" intersects with the "semi-circular chamber" and the 1st and 2nd "sub-outlet channels" [*Parikesit et al., 2005*]. We therefore focus our observations in this study on the same region, which is also shown as the white rectangle in Figure 5.1(b). Figure 5.2 shows two examples of the sets of pathlines of DNA molecules driven by an electric field of V = 15.3 V (DC). In Figure 5.2, the top pathline set is of λ-DNA molecules, while the bottom pathline set is the result from T4GT7-DNA molecules. These pathlines were obtained by simple addition of all the images in each dataset.

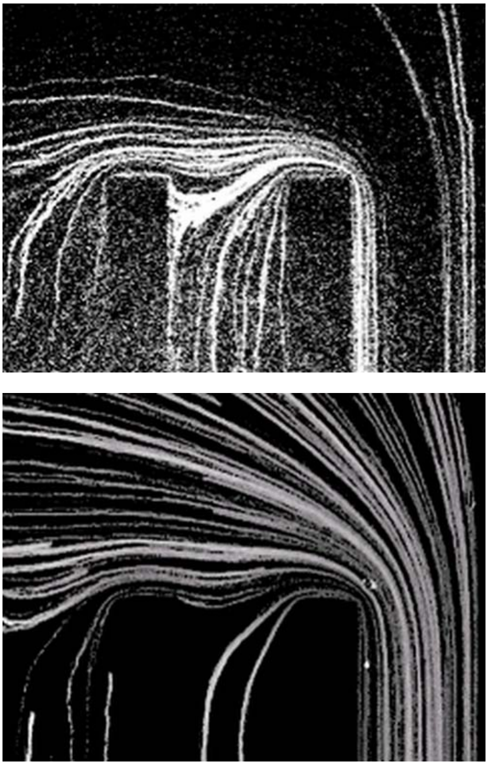

Figure 5.2. Two examples of the sets of pathlines of DNA molecules (shown as white lines) flowing at the region of observation, where the value of applied electric field is V = 15.3 V (DC). Top: the pathlines of λ-DNA molecules. Bottom: the pathlines of T4GT7-DNA molecules.

It is very difficult to compare and analyze the two example images in Figure 5.2 using only visual inspection. For example, qualitative comparison between Figure 5.2 and Figures 4.2-4.3 show similar pathlines, even though quantitatively this may not be the case. Therefore we perform some image analysis steps on the measured fluorescent images using our image processing toolbox DIPimage [*Luengo et al., 1999*]. First, we create a “background image” by averaging all images in one particular measurement. The “background image”, Image_{bg}, can be expressed mathematically as:

$$\text{Image}_{bg} = \frac{1}{n}\sum_{j=1}^{n}\text{Image}_{j} \,, \qquad (5.1)$$

where n is the number of images in the analyzed measurement data ($n \approx 1000$). The “background image” is then subtracted from each of the images in that measurement in order to remove unwanted signals such as auto-fluorescence from the channel walls and static objects in the channels. Afterwards, DNA molecules in each resulting images are segmented from the background using a fixed threshold algorithm [*Young et al., 1998*]. The analysis is only done in a region-of-interest

(ROI), which is defined as a rectangle around a single DNA molecule of interest, where the position of the molecule is determined by measuring the center-of-gravity across the ROI. In order to track the moving molecule, the ROI is also moved along with the molecule. This is done by using the measured molecule's center-of-gravity to specify the center of the moved ROI. Individual pathlines are then determined by tracking the molecules through the image sequence in the measured data.

V.3 Results and discussions

For our analysis, we need to consider all the electrokinetic forces involved in the transport of the DNA molecules. As the electric field is applied, the negatively charged DNA molecules are driven from the negative electrode towards the positive electrode by electrophoresis, while the liquid surrounding the DNA and filling the channels flows in the opposite direction due to electro-osmosis. On top of that, the combination between DNA molecules and their surrounding counter-ions can be polarized and, where an electric field gradient exists, the DNA molecule can be attracted to the region with the highest electric field gradient because of dielectrophoresis [*Chou et al., 2002*]. Hence electrophoresis and electro-osmosis only determine the velocity and general pathline of the DNA molecules, while dielectrophoresis can alter the details of the pathlines of the DNA molecules. The total velocity field across the channels is the sum of the electroosmotic, electrophoretic, and dielectrophoretic velocity fields:

$$\mathbf{v} = \mathbf{v_{EO}} + \mathbf{v_{EP}} + \mathbf{v_{DEP}} = \mu_{EK}\mathbf{E} + \mu_{DEP}\nabla\left|\mathbf{E}\right|^2, \qquad (5.2)$$

with μ_{EK} as the electroosmotic-plus-electrophoretic mobility and μ_{DEP} as the dielectrophoretic mobility [*Cummings et al., 2003*].

We have performed a two-dimensional finite-element numerical computation of $|\mathbf{E}|^2$ through the channels, as shown in Figure 5.3, using the Electrostatics Module in Comsol Multiphysics 3.3 (Comsol, Burlington, MA, USA). The mesh size is made uniform and sufficiently small throughout all the channels, such that the $|\mathbf{E}|^2$ values do not change anymore when the mesh is refined further. For the boundary conditions, we assume total insulation in all the channel walls and apply appropriate voltages to the inlet and outlet ports. Moreover, because infinitely sharp corners cannot be practically achieved during the fabrication, we use rounded channel corners in the simulation. We observed that this does not significantly change the qualitative distribution of $|\mathbf{E}|^2$ in the whole device, except very near the corner indicated by the arrow in Figure 5.3, where sharp corners would result in a non-realistic singularity at that corner, while rounded corners result in a more smooth distribution of $|\mathbf{E}|^2$. From Figure 5.3, we can also see that the region where we have non-zero *gradient* of $|\mathbf{E}|^2$, i.e. where dielectrophoresis could alter the pathlines of DNA molecules (see equation 5.2), is *around* the corner indicated by the arrow.

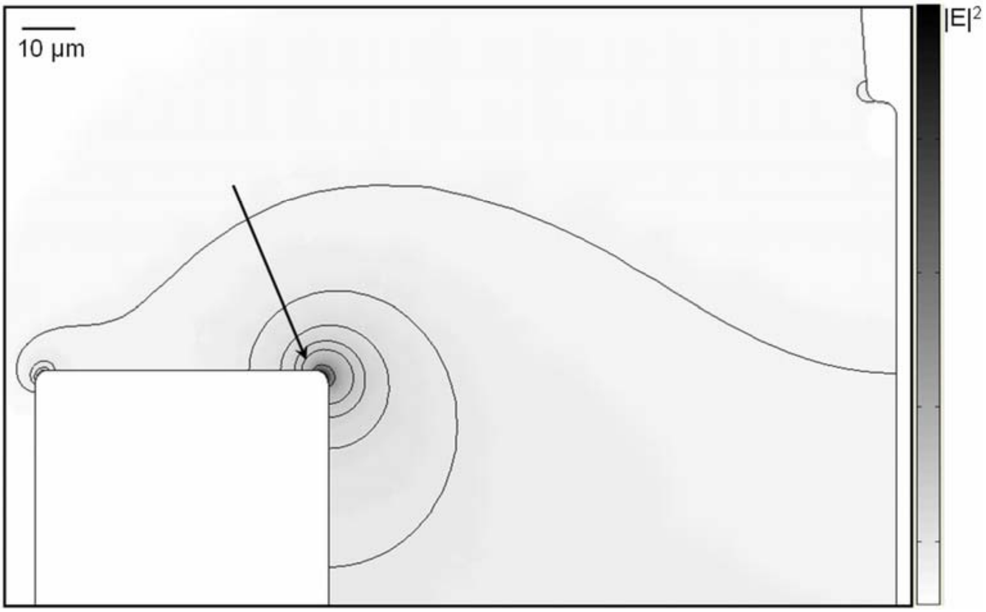

Figure 5.3 A two-dimensional numerical simulation of the electric field squared, $|\mathbf{E}|^2$, specifically in the region of our experimental observation, i.e. at the end of the "inlet channel". The colorbar has maximum and minimum values of $2.233*10^6$ V^2 and $1.011*10^{-8}$ V^2, respectively. Several iso-level contours of $|\mathbf{E}|^2$ are also shown (for $|\mathbf{E}|^2$ equal to $1*10^6$, $5*10^5$, $4*10^5$, $3*10^5$, $2*10^5$, and $1*10^5$ V^2) only for visual aid. The dark region at one of the wall corners, indicated by the arrow, shows the location with the highest value of $|\mathbf{E}|^2$ throughout the branched U-turn nanofluidic channel. The region with non-zero gradient of $|\mathbf{E}|^2$ is around that corner. The scale bar represents 10 μm.

The next step in the analysis is to quantitatively compare and analyze each pathline in all measurements and for that purpose we define two parameters as shown in Figure 5.4. First we measure the "start distance", r_{start}, as the distance along the x-axis from the first corner in the walls (illustrated in Figure 5.4 with the dashed lines, separating the inlet, semi-circular chamber, and the 1st sub-outlet). Then we also measure the "finish distance", r_{finish}, as the distance along the y-axis from the second corner in the same walls. The distances are then calculated using a conversion factor of 1 pixel width = 1.29 μm (taking into account the 4x4-pixels binning and the 20x lens we use in the experiments; this is also confirmed experimentally by using the known width of the inlet channel).

The electric field applied during the measurements can be expressed by the equation [$V=A \sin(2\pi ft) + B$], where f and A are the frequency and amplitude of the AC signal, respectively, while B is the DC offset superimposed on the AC signal. The total contour length of the channels between the inlet and outlet ports, where the electric fields are applied, is approximately 2 cm. Table 5.1 shows the parameters chosen for the experiments, resulting in 10 datasets. The plots in Figure 5.5 and Figure 5.6 summarize the results of the experiments. In order to test the repeatability of our observations, we perform a second set of experiments more than one month after the first set of experiments, using different microchips. In the plots shown in Figures 5.5 and 5.6 we therefore use the notations “1” and “2” on the datasets, which indicate the first and second set of experiments, respectively.

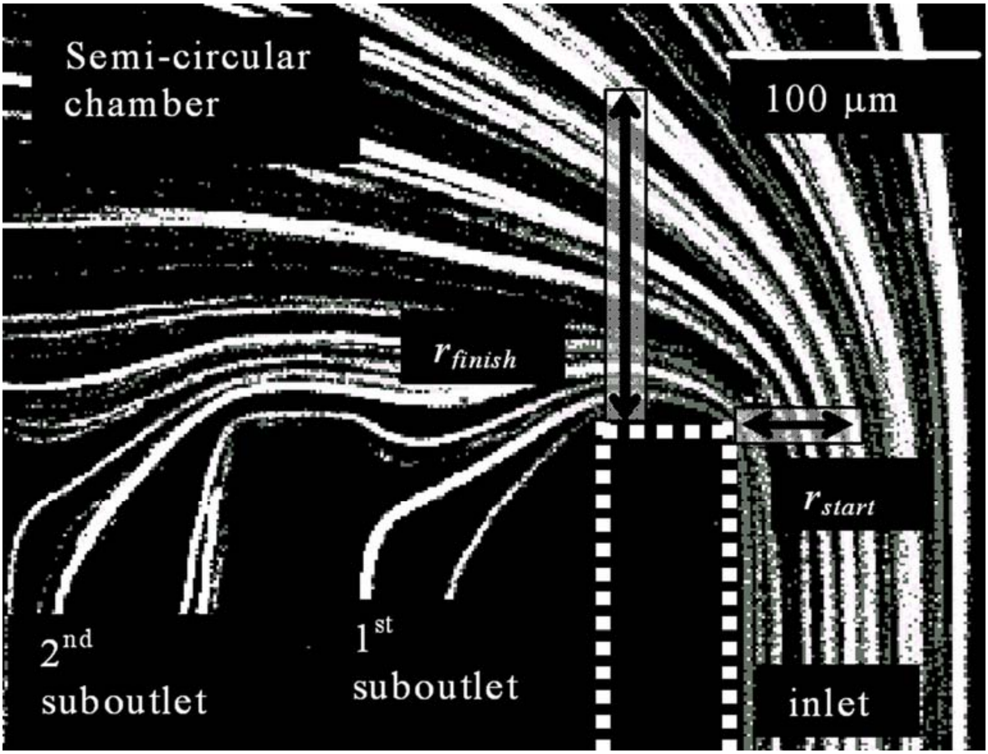

Figure 5.4. The parameters used in the analysis are: the “start distance”, r_{start}, and the “finish distance”, r_{finish}, measured from the corners of the walls (here, the walls are illustrated with the dashed lines, separating the inlet, the semi-circular chamber, and the 1st sub-outlet). The scalebar represents 100 µm.

Table 5.1 List of parameter choices in the experiments, along with the respective dataset names and colours used in the plots.

DNA molecules	Electric field: *A* = 0 V *f* = 0 Hz *B* = 7.5 V	Electric field: *A* = 0 V *f* = 0 Hz *B* = 15.3 V	Electric field: *A* = 0 V *f* = 1 Hz *B* = 15.3 V	Electric field: *A* = 14 V *f* = 1 kHz *B* = 15.3 V	Electric field: *A* = 14 V *f* = 1 MHz *B* = 15.3 V
λ (48.5 kbp)	Dataset A (black)	Dataset B (black)	Dataset C (black)	Dataset D (black)	Dataset E (black)
T4GT7 (165.6 kbp)	Dataset F (grey)	Dataset G (grey)	Dataset H (grey)	Dataset I (grey)	Dataset J (grey)

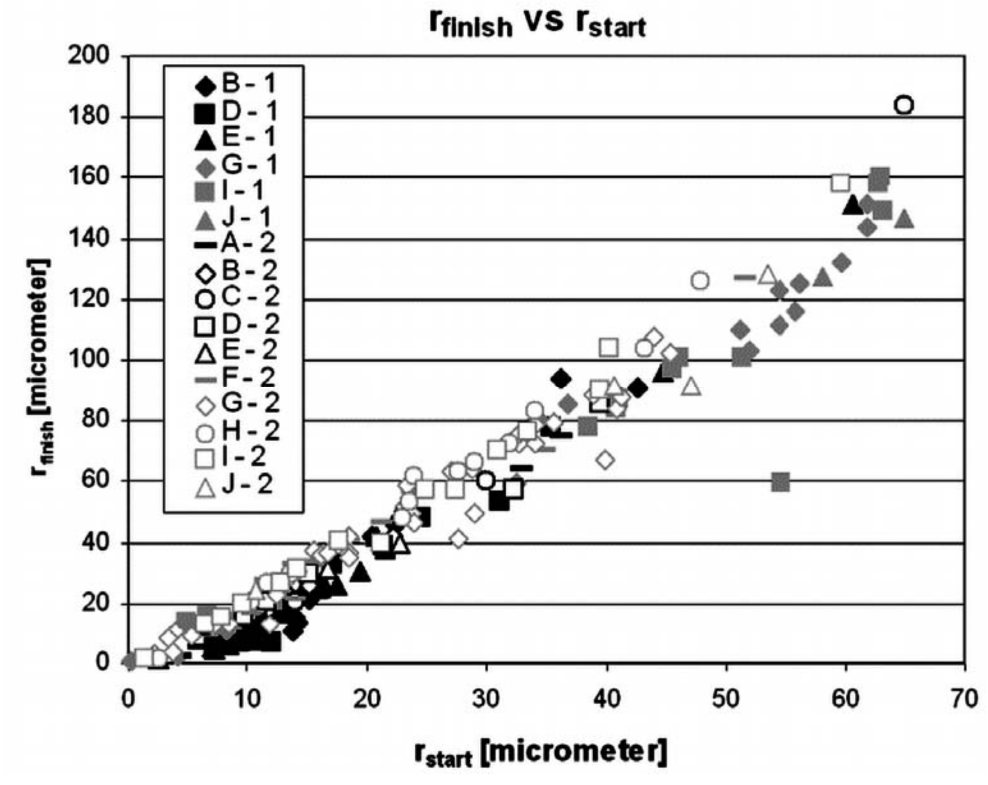

Figure 5.5. The plot of r_{finish} vs r_{start} for all datasets.

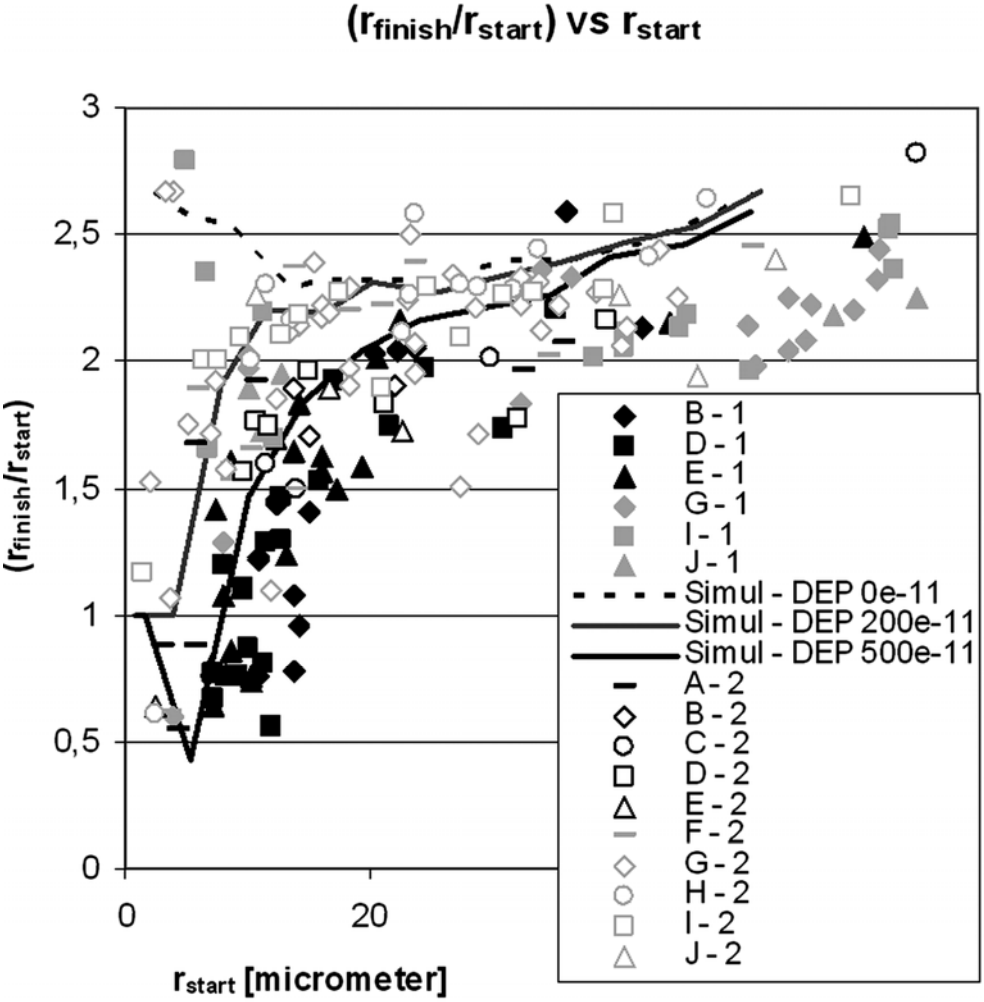

Figure 5.6 The plot of (r_{finish}/r_{start}) vs r_{start} along with the simulated pathlines for all r_{start} values.

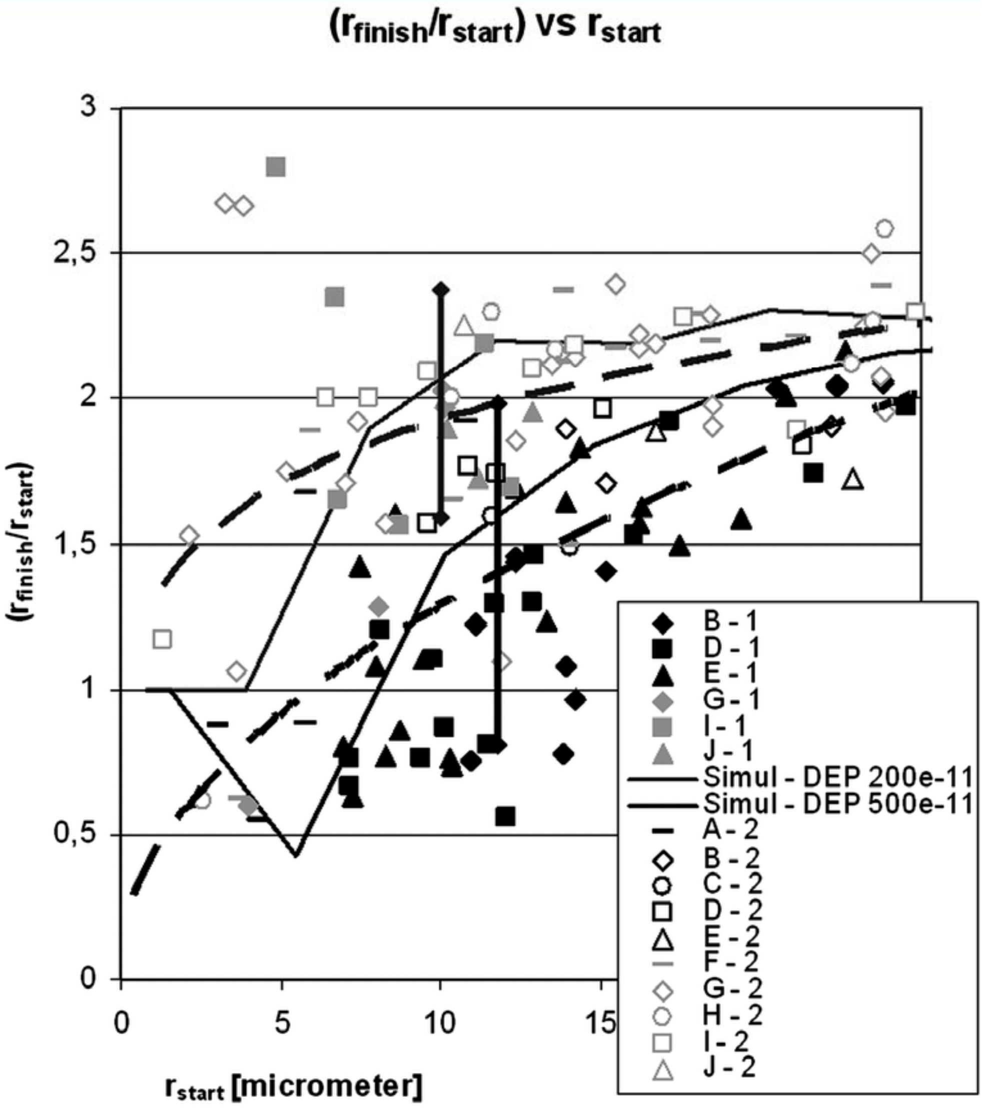

Figure 5.7 The plot of (r_{finish}/r_{start}) vs r_{start} along with the simulated pathlines, particularly for $r_{start} < 25$. The dashed lines and error-bars represent trend lines and error margins of the experimental data (only for visual aid).

In Figure 5.5, we plot r_{finish} vs r_{start} for all datasets. If size-based DNA sorting occurs, then λ-DNA and T4GT7-DNA will systematically have different pathlines, and consequently have different values of r_{finish}, even though they start at the same position in the inlet and have the same value of r_{start}. Let us now compare the black markers (datasets A-E, i.e. λ-DNA in 400-nm channels) and the grey markers (datasets F-J, i.e. T4GT7-DNA in 400-nm channels) in Figure 5.5. Particularly for

r_{start} < ~25 μm, the black markers consistently have r_{finish} values lower than the grey markers. Physically this indicates that we can sort a mix of λ-DNA and T4GT7-DNA in 400-nm deep channels for r_{start} < ~25 μm, because for the same values of r_{start} their pathlines end up with different r_{finish}.

Meanwhile, Figures 5.6 and 5.7 show the plots of (r_{finish}/r_{start}) vs r_{start} for the same datasets. Compared to the plot in Figure 5.5, these plots allow us to take a closer look at the trends of the datasets. The same comparison between the black markers and the gray markers can then be repeated. Again, we see that for r_{start} < ~25 μm the black markers have lower values of (r_{finish}/r_{start}) than the grey markers. This confirms our remark above that for r_{start} < ~25 μm we can sort a mix of λ-DNA and T4GT7-DNA inside the channels. Using the same numerical computation as was used to plot Figure 5.3, we also simulate the electrokinetic DNA pathlines. In the simulation, we adjust the ratio of dielectrophoretic mobility, μ_{DEP}, and electrokinetic mobility, μ_{EK}, as defined in equation 5.2. The simulation results are also plotted in Figures 5.6 and 5.7, for $\rho_\mu=(\mu_{DEP}/\mu_{EK})$ equal to zero (i.e. when there is no dielectrophoresis effect in the system; shown as black box with lines), $\rho_\mu=200\text{x}10^{-11}$ m.kg.s^{-7}.A^{-3} (shown as grey line), and $\rho_\mu=500\text{x}10^{-11}$ m.kg.s^{-7}.A^{-3} (shown as black line); the latter two simulation cases represent positive dielectrophoresis, where the DNA electrokinetic pathlines are shifted toward the highest electric field gradient indicated in Figure 5.3. Comparison between the simulation and experimental data in Figures 5.6 and 5.7 shows that the simulation of $\rho_\mu=200\text{x}10^{-11}$ m.kg.s^{-7}.A^{-3} matches the datasets with black markers, while the simulation of $\rho_\mu=500\text{x}10^{-11}$ m.kg.s^{-7}.A^{-3} matches the datasets with grey markers (In Figure 5.7, we also show trend lines and error margins of the experimental data, only for visual aid). This shows that the pathlines of the larger DNA (T4GT7-DNA) are attracted by dielectrophoresis toward the walls corner less strongly than the pathlines of the smaller DNA (λ-DNA). These observations are surprising, because Chou et al. reported that, in contrast to our observations, dielectrophoretic effects on DNA molecules increase when the DNA size is increased [*Chou et al., 2002*]. A possible explanation is that as the DNA molecules pass the sharp corners at the U-turn, almost all of the monomers in the shorter DNA (λ-DNA) are affected by the attracting dielectrophoretic force while only some monomers in the longer DNA (T4GT7-DNA) are affected by the same force. The dielectrophoresis effects are therefore rendered to be less effective on the longer DNA than on the shorter DNA. On top of that, we also have to note that our experiments are done in a nanofluidic setup, while Chou et al. used a microfluidic setup which has a much smaller confinement effect on the DNA molecules.

We have shown above that DNA molecules can be sorted based on their size particularly for r_{start} < ~25 μm, i.e. for pathlines that are close enough to the highest grad($|\mathbf{E}|^2$) value in the channel (see Figure 5.7). This indicates that, for the first time, size-based DNA sorting can be done in a continuous, sieve-less, manner. The sorting is enabled by dielectrophoretic forces, which alter the DNA pathlines. Hydrodynamic filtration [*Yamada et al., 2006*], which is an alternative possible mechanism for sorting around channel corners, could not explain our experimental data. In hydrodynamic filtration, as two particles with different sizes (but with the same distance between the channel wall and the particles' *nearest-edge*) pass around a corner, the smaller particle tend to stay closer to the wall (and consequently, tend to make a sharper bend) than the bigger particle, due to the steric effects between the particles and the channel walls. The same effects, however, imply that both particles have already different distances between the channel wall and the particles' *center-of-gravity*, even before they pass the corner. Because in our image analysis we only compare different pathlines for the same r_{start} (i.e. the same distances between the channel wall and the particles' center-of-gravity), we manage to ensure that our observed sorting is not due to hydrodynamic filtration.

Our results are novel compared to the previous results of other authors, where dielectrophoresis has been used either for continuous sorting but only for cells or for spherical beads [*Cummings et al., 2003*], or for manipulating DNA but only by trapping and not by continuous sorting [*Chou et al., 2002*; *Regtmeier et al., 2007*]. Meanwhile, for r_{start} > ~25 μm, no sorting can effectively be done because the pathlines are too far away from the corners in the channel walls, hence no significant dielectrophoresis effect exists. We should mention, however, that the dimensions and configurations of the channels in our branched U-turn nanofluidic channels are not yet optimised for an effective sorting operation. To do sorting more effectively, the following geometry modification of the channels could be done (see Figure 5.8): (1) connect a three-branch channel prior to the inlet channel, as in cytometry devices [*Wang et al., 2004*], to allow sheath flows to control the r_{start} of the DNA molecules coming to the inlet channel; (2) make the width of the inlet channel significantly narrower, in order to ensure all DNA molecules have pathlines sufficiently close to the corners in the channel walls; and (3) connect several identical branched U-turn channels in series, so that the sorting capability can be amplified to obtain a higher separation resolution. This would be particularly useful if we need to sort a mix of more than two types of DNA molecules. On top of that, another possible improvement would be to take into account the stagnation points of the pathlines. These points are shown in Figures 5.2 and 5.4 as locations where two adjacent pathlines split toward two different sub-outlets. By re-configuring the sub-outlets, such that the stagnation points are positioned at the walls between the sub-outlets (rather than inside the sub-outlets themselves as in the present case), sorting between pathlines toward different sub-outlets could be performed more optimally.

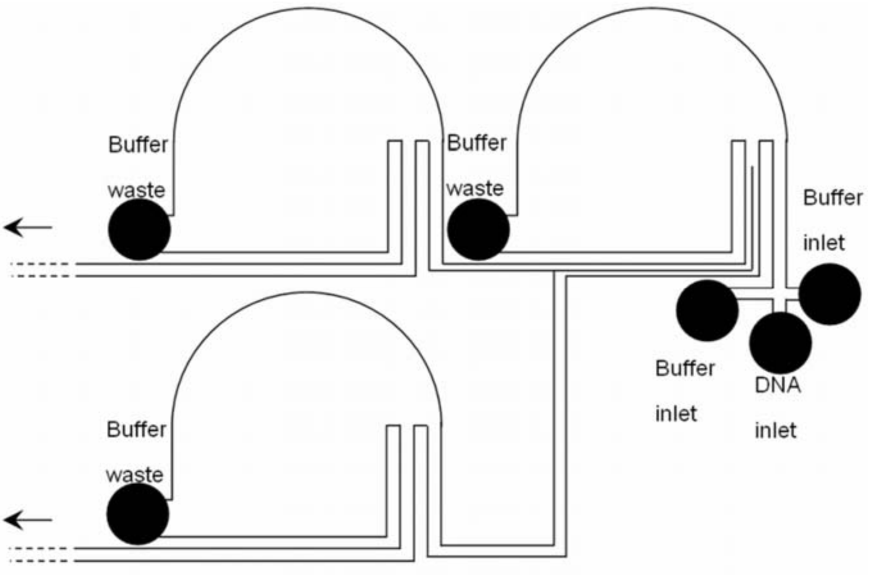

Figure 5.8 A schematic view of the proposed lateral geometry (i.e. along the x- and y-axis) modification of the channel for a continuous, sieve-less, DNA sorting operation. The arrows indicate that the DNA molecules and the buffer solution can further go to the next stage of the cascaded device before eventually go to DNA waste-ports and buffer waste-ports.

In order to see the effect of modifying the applied electric fields, we can compare the trends of datasets in each colour of the markers (i.e. comparison between datasets A-E among the black markers, and between datasets F-J among the grey markers). The plots in Figures 5.5, 5.6, and 5.7 show that there is no clear distinction between the trends of datasets in each colour of the markers. In other words, we do not observe any significant effect by changing the applied electric fields in our experiment. However, the AC fields in our experiments only have a frequency of 1 Hz, 1 kHz or 1 MHz. Further investigations could also be done with higher frequencies, because the dielectrophoresis effect has been reported to increase when the AC frequency is increased [*Chou et al., 2002*]. Meanwhile, our results from the experiments using DC fields also indicate that DNA molecules experience positive dielectrophoresis, even though there is no periodic modulation of the electric field as typically caused by AC fields. This could be explained by the highly non-uniform ion and counter-ion concentrations along the nanofluidic channel depth, particularly when the depth is sufficiently small such that the electric double layer from the upper and lower channel walls are very close to each other, as in our case. This would cause significant dynamic transverse transport of the ions along the channel depth (i.e. the z-axis) [*Pennathur et.al., 2005*], and consequently the combination of DNA molecules and their surrounding counter-ions are perpetually polarized along the channel depth (i.e. the z-axis) [*Baldessari et al., 2006*], even though no AC fields are applied between the channel inlet and outlet. Any significant electric field gradient, such as caused by the sharp corner at the U-turn in our nanochannels (see Figure 5.3), would therefore cause positive dielectrophoresis to the DNA molecules regardless of whether the applied electric fields are AC or DC.

V.4 Conclusion

In this chapter, we demonstrate for the first time that sieve-less U-turn nanochannels can induce size-dependent electrokinetic pathlines of DNA molecules. In our experiments, we use λ (48.5 kbp) and T4GT7 (165.6 kbp) DNA molecules flowing continuously inside our 400 nm deep channels. Meanwhile, numerical simulations indicate that the observed pathlines can be explained by dielectrophoresis, which occurs even under DC electrical fields, presumably due to the nanofluidic confinement. Both our experimental and numerical observations indicate that U-turn nanochannels allow size-based DNA separation to be operated in a sieve-less and continuous manner, hence importantly enabling us to avoid complicated sieve designs while obtaining high throughput in Lab-on-a-Chip systems.

We expect that these results will stimulate more investigation into continuous and sieve-less separation of DNA molecules in nanofluidic channels. Moreover, the observations in our experiments should also stimulate further investigations on the dielectrophoresis of DNA molecules in nanofluidic channels. The key concept introduced in this chapter is that electrokinetic forces inside nanofluidic channels can be engineered, for example, by using the branched U-turn channel geometry, to continuously alter the pathlines of DNA molecules. Even though we only use DNA molecules in this study, the concept should also be valid for any other polarizable biological molecules that can be manipulated with dielectrophoresis. Moreover, the concept can also be extended to perform free-flow dielectrophoretic separation on cells and other polarizable micro-particles [*Parikesit et al., 2007a*].

V.5 Epilogue

Related to this study, we have performed another set of experiments using a different set of microchips, fabricated by Micronit Microfluidics B.V. (Enschede, The Netherlands). The channels on these microchips have exactly the same lateral geometry (i.e. along the x-axis and y-axis) as the microchips used in the experiments above. They do not, however, have a layer of a:Si in between the upper and lower layer of glass wafers, because they are bonded using direct bonding rather than anodic bonding. On top of that, the channel depth in these channels (i.e. the z-axis) is 500 nm as opposed to 400 nm.

The results are shown in Figure 5.9. Here we see that (r_{finish}/r_{start}) is in general shifted toward larger values, compared to our previous results shown in Figure 5.6.

The datasets in Figure 5.9 can be described by a finite-element numerical calculation that assumes we have a negative dielectrophoresis with a (μ_{DEP}/μ_{EK}) of -100x10^{-11} m.kg.s^{-7}.A^{-3} (shown as black triangles with blue lines), as opposed to positive dielectrophoresis like in Figure 5.6; although the simulation seems to match the datasets of T4GT7-DNA (grey markers) better than it matches the datasets of λ-DNA (black markers). At this point of writing we do not yet have a physical model for these observed phenomena.

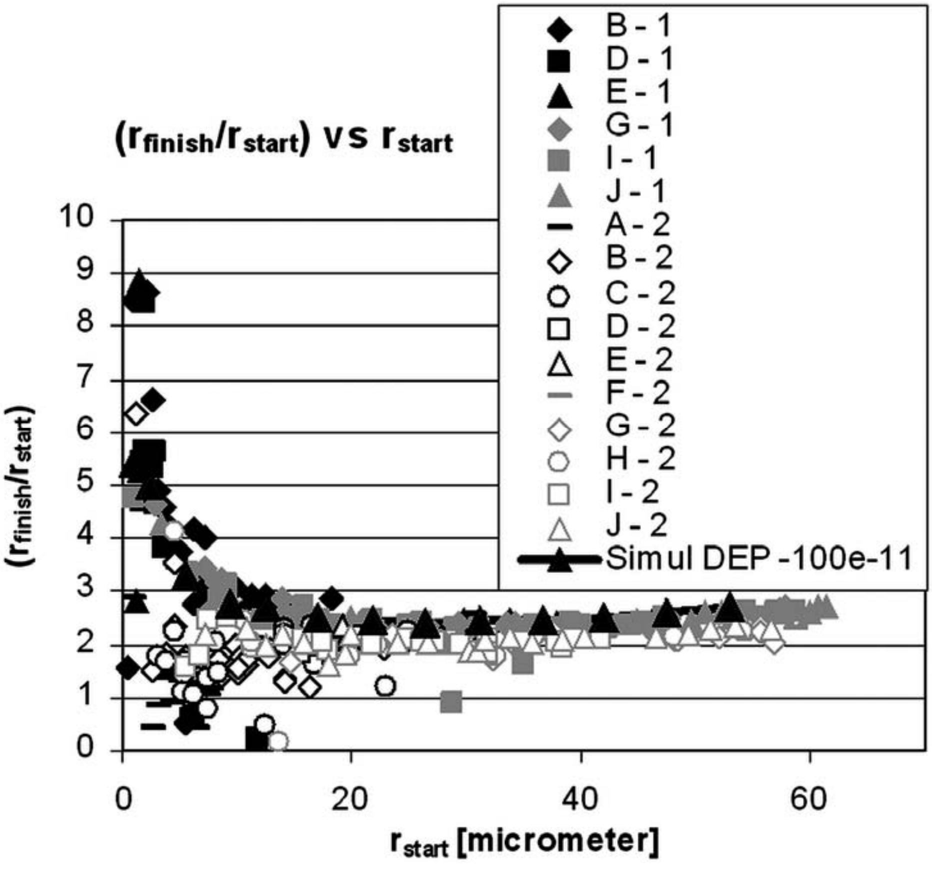

Figure 5.9 The plot of (r_{finish}/r_{start}) vs r_{start} for the datasets of experiments using the microchips fabricated by Micronit Microfluidics B.V., along with the simulated pathlines for negative dielectrophoresis with a (μ_{DEP}/μ_{EK}) of -100x10^{-11} m.kg.s^{-7}.A^{-3}.

VI. General conclusions

In this chapter we draw some general conclusions from the research reported in this thesis. First we review the results with respect to the research questions posed in Chapter 1. Afterwards we make some recommendations, based on our results and on the challenges we faced during the investigation, for future research in this direction.

VI.1 Review of results

In this research we investigate the possibility of using nanofluidic channels with a novel “branched U-turn” geometry to perform a separation of individual DNA molecules. If separation can be done across the channel width, instead of along the channel length as typically done, the unwanted “race-track” effect can be avoided while the continuous operation would enable a high-throughput analysis. In this study, the channel depth is less than 1 micrometer, while the channel lengths and widths are in the range of 100 micrometers. The **research questions** that have been investigated are as follows:

1. How does the fluid flow behave when various types of electric fields are applied across these channels?
2. How do the pathlines of individual DNA molecules behave inside the confining nanofluidic channels?
3. Can we use these channels as novel devices to sort and characterize single DNA molecules?

In Chapter 4 we studied the **first question** by investigating and analyzing the electro-osmotic flow inside the nanofluidic channels. In the experiments, we use distilled water as the liquid in which we add 110 nm diameter fluorescent beads employed as tracer-particles inside 150 nm deep nanofluidic channels. From the results we can characterize the pathlines and velocity distribution of the fluid flow. Due to the complex geometry of the channel, the electro-osmotic flow cannot be calculated analytically. Therefore we use numerical flow simulations to build our model. The quasi-two-dimensional geometry of our channels implies that we have a Hele-Shaw condition, where steady and vertically averaged flow pattern is described by potential flow and can be easily computed (without taking Brownian motion into account). Comparison between the experimental data and the simulation results give a very good agreement, where the deviation can be explained by the measured Brownian motion of the tracer-particles which was not incorporated in the simulation.

The **second question** was investigated in Chapter 5. Experiments are performed with two types of dsDNA molecules, λ (48.5 kbp) and T4GT7 (165.6 kbp), using channels with depths of 400 nm. We observe that the electrokinetic pathlines of the DNA molecules depends on the DNA size. We use numerical simulation to calculate the distribution of electrokinetic forces in the channels, which can explain the observed experimental phenomena.

The results of Chapter 5 also indicate that, for the first time, size-based separation of DNA molecules can be done in a continuous, sieve-less, manner. This is related to our **third question**. By using the nanofluidic channel geometry, we can configure the electric field distribution in the channels and manipulate the electrokinetic forces to influence the pathlines of the DNA molecules. The same results can be expected not only on DNA molecules, but also on any other polarizable biological molecules that can be manipulated using dielectrophoresis.

VI.2 Recommendations

Early in our investigation, we discovered a persistent problem in the channels fabricated with embedded electrodes (see Chapter 3). There was fluid leakage in the fabricated channels that prevented us from performing well-controlled experiments. Because of our limited time and research scope, we did not pursue the fabrication problem. Nevertheless, doing that in the future would be very beneficial because the embedded electrodes would provide us with a lot more freedom in the experiments, particularly in controlling the electro-osmosis, electrophoresis, and dielectrophoresis inside the nanofluidic channels.

The results from Chapter 4 highlighted how the Brownian motion plays a significant role in the distribution of pathlines inside the channels. We would, therefore, recommend a future research to alter and optimize the design of the channels, in particular the design of the sub-outlet channels. Because it takes a longer time for particles to follow the pathlines toward the last sub-outlets than to follow the pathlines toward the first sub-outlets, a larger deviation due to Brownian motion is expected for the previous case than for the latter one. To compensate this, the opening of the last sub-outlets could then be made wider than the opening of the first sub-outlets, such that all pathlines remain captured in the desired sub-outlets regardless the deviation from Brownian motion. This is shown in Figure 6.1. In general, conformational mapping could be used to compute the Hele-Shaw potential flow in our channels and transform them into more simple devices with an equal level of desired performances [*Kundu and Cohen, 2004*].

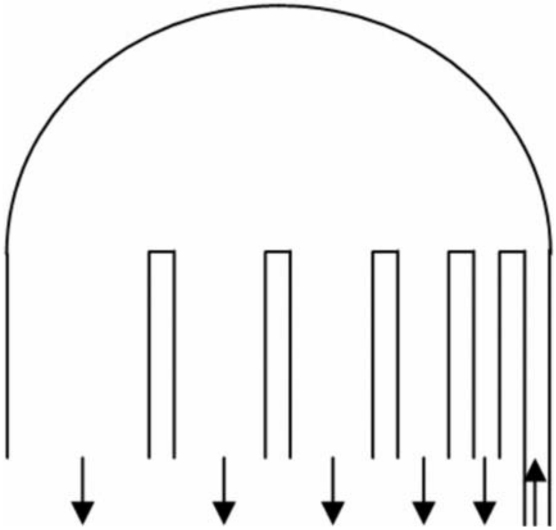

Figure 6.1 A schematic view of the proposed lateral geometry (i.e. along the x- and y-axis) modification of the channel to compensate for the random Brownian motion, such that the distribution of pathlines from the inlet channel to all sub-outlet channels would be the same. Note that the sub-outlets channels further away from the inlet channel are made wider, because the Brownian-motion-related spreading of the pathlines is expected to be larger for longer pathlines.

A similar recommendation, i.e. optimization of the channel geometry, can also be made with respect to the results in Chapter 5. In that chapter, we showed that dielectrophoresis could be used not only to trap DNA molecules (as reported by other researchers) but also to alter the pathlines of the DNA molecules. In order to improve the dielectrophoretic force field in the channels and to sort the molecules more efficiently, the shape and configurations of the sub-outlet channels and of the corners at the end of the inlet channel could be modified. This is shown in Figure 5.8. Moreover, it would also be useful to study the phenomena using a more advanced numerical calculation. For example, a three-dimensional simulation could be performed to include not only the electrokinetic forces in the channels (as has been presented in Chapter 5) but also how the conformation of each DNA molecules would be influenced by many parameters, e.g. the sharpness of the corners in the channels and the rate of the dynamic transverse transport of the ions in the very shallow channels.

Our final recommendations are to extend this investigation to molecules other than DNA and to study in more details how those molecules can be controlled using dielectrophoresis in nanofluidic channels. By applying the separation scheme to separate and analyze the properties of proteins and other biomolecules, the scheme could be developed for a range of applications. The ultimate research vision is to integrate the separation scheme with other analytical devices to form a complete Lab-on-a-Chip system, which would enable us to extract, separate, and analyze biomolecules directly from individual cells.

References

[*Bakajin et.al., 2001*] O. Bakajin, T.A. Duke, J. Tegenfeldt, C-F. Chou, S.S. Chan, R.H. Austin, E.C. Cox, "Separation of 100-kilobase DNA molecules in 10 seconds", Analytical Chemistry (2001) 73:6053-6056.

[*Baldessari et.al., 2006*] F. Baldessari, J.G. Santiago, "Electrophoresis in nanochannels: brief review and speculation", Journal of Nanobiotechnology (2006) 4:12-17.

[*van den Berg et al., 2006*] A. van den Berg, P. Bergveld, “Labs-on-a-Chip: origin, highlights and future perspectives - On the occasion of the 10th μTAS conference”, Lab on a Chip (2006) 6:1266-1273.

[*Bianchi et al., 2000*] F. Bianchi, R. Ferrigno, H.H. Girault, “Finite Element Simulation of an Electroosmotic-Driven Flow Division at a T-Junction of Microscale Dimensions”, Analytical Chemistry (2000) 72:1987-1993.

[*Brask et al., 2002*] A. Brask, G. Goranovic, H. Bruus, “Theoretical analysis of the low-voltage cascade electro-osmotic pump”, Sensors and Actuators B: Chemical (2002) 92:127-132.

[*Burgreen et al., 1964*] D. Burgreen, F.R. Nakache, “Electrokinetic flow in ultrafine capillary slits”, Journal of Physical Chemistry (1964) 68:1084-1091.

[*Cabodi et al., 2002*] M. Cabodi, S.W.P. Turner, H.G. Craighead, “Entropic recoil separation of long DNA molecules”, Analytical Chemistry (2002) 74:5169 -5174.

[*Chan et al., 2006*] Y.C. Chan, Y. Zohar, Y-K. Lee, “Nonlinear electrophoretic mobility of large DNA molecules in microsystems with sub-micron pillar arrays”, Proceedings of MEMS 2006 Istanbul, IEEE, 438-441.

[*Chou et.al., 1999*] C-F. Chou, O. Bakajin, S.W. Turner, T.A.J. Duke, S.S. Chan, E.C. Cox, H.G. Craighead, R.H. Austin, "Sorting by diffusion: an asymmetric obstacle course for continuous molecular separation", PNAS (1999) 96:13762-13765.

[*Chou et al., 2002*] C-F Chou, J.O. Tegenfeldt, O. Bakajin, S.Y. Chan, E.C. Cox, N. Darnton. T. Duke, R.H. Austin, “Electrodeless Dielectrophoresis of Single and Double Stranded DNA”, Biophysical Journal (2002) 83:2170-2179.

[*Cohen et al., 2005*] A.E. Cohen, W.E. Moerner, “Method for trapping and manipulating nanoscale objects in solution”, Applied Physics Letters (2005) 86:093109.

[*Conlisk et al., 2002*] A.T. Conlisk, J. McFerran, “Mass Transfer and Flow in Electrically Charged Micro- and Nanochannels”, Analytical Chemistry (2002) 74:2139-2150.

[*Cross et al., 2007*] J.D. Cross, E.A. Strychalski, H.G. Craighead, “Size-dependent DNA mobility in nanochannels”, Journal of Applied Physics (2007) 102:024701.

[*Cummings et al., 2000*] E.B. Cummings, S.K. Griffiths, R.H. Nilson, P.H. Paul, “Conditions for Similitude between the Fluid Velocity and Electric Field in Electroosmotic Flow”, Analytical Chemistry (2000) 72:2526-2532.

[*Cummings et.al., 2003*] E.B. Cummings, A.K. Singh, “Dielectrophoresis in microchips containing arrays of insulating posts: theoretical and experimental results”, Analytical Chemistry (2003) 75:4724-4731.

[*Dittrich et al., 2005*] P.S. Dittrich, A. Manz, “Single-Molecule Fluorescence Detection in Mircofluidic Channels - the Holy Grail in µTAS?”, Analytical and Bioanalytical Chemistry (2005) 382:1771–1782.

[*Dutta et al., 2002a*] P. Dutta, A. Beskok, T.C. Warburton, “Electroosmotic Flow Control in Complex Micro-Geometries”, Journal of Microelectromechanical Systems (2002) 11:36-44.

[*Dutta et al., 2002b*] P. Dutta, A. Beskok, T.C. Warburton, “Numerical Simulation of Mixed Electroosmotic / Pressure Driven Microflows”, Numerical Heat Transfer, Part A (2002) 41:131-148.

[*Eijkel et al., 2005*] J.C.T. Eijkel, A. van den Berg, “Nanofluidics: what is it and what can we expect from it?”, Microfluidics and Nanofluidics (2005) 1:249-267.

[*Eijkel et.al., 2006a*] J.C.T. Eijkel, A. van den Berg, “Nanotechnology for membranes, filters and sieves”, Lab on a Chip (2006) 6:19-23.

[*Eijkel et al., 2006b*] J.C.T. Eijkel, A. van den Berg, “Young 4ever - the use of capillarity for passive flow handling in lab on a chip devices”, Lab on a Chip (2006) 6:1405 – 1408.

[*Faber, 1995*] T.E. Faber, “Fluid Dynamics for Physicist”, Cambridge University Press, 1995.

[*Foquet et al., 2004*] M. Foquet, J. Korlach, W.R. Zipfel, W.W. Webb, H.G. Craighead, “Focal volume confinement by submicrometer-sized fluidic channels”, Analytical Chemistry (2004) 76:1618-1626.

[*Fu et.al., 2006*] J. Fu, J. Yoo, J. Han, “Molecular Sieving in Periodic Free-Energy Landscapes Created by Patterned Nanofilter Arrays”, Physical Review Letters (2006) 97:018103.

[*Fu et.al., 2007*] J. Fu, R.B. Schoch, A.L. Stevens, S.R. Tannenbaum, J. Han, "A patterned anisotropic nanofluidic sieving structure for continuous-flow separation of DNA and proteins", Nature Nanotechnology (2007) 2:121-128.

[*Garcia et al., 2005*] A.L. Garcia, L.K. Ista, D.N. Petsev, M.J. O’Brien, P. Bisong, A.A. Mammoli, S.R.J. Brueck, G.P. Lopez, “Electrokinetic molecular separation in nanoscale fluidic channels”, Lab on a Chip (2005) 5:1271–1276.

[*Han et al., 1999*] J. Han, S.W. Turner, H.G. Craighead, “Entropic trapping and escape of long DNA molecules at submicron size constriction”, Physical Review Letters (1999) 83:1688-1691.

[*Han et.al., 2000*] J. Han, H.G. Craighead, "Separation of long DNA molecules in a microfabricated entropic trap array", Science (2000) 288:1026-1029.

[*Huang et al., 2002*] L.R. Huang, J.O. Tegenfeldt, J.J. Kraeft, J.C. Sturm, R.H. Austin, E.C. Cox, “A DNA prism for high-speed continuous fractionation of large DNA molecules”, Nature Biotechnology (2002) 20:1048 – 1051.

[*Huang et.al., 2004*] L.R. Huang, E.C. Cox, R.H. Austin, J.C. Sturm, "Continuous particle separation through deterministic lateral displacement", Science (2004) 304:987-990.

[*Hunter, 2001*] R.J. Hunter, “Foundations of Colloid Science”, Oxford University Press, 2001.

[*Jin et al., 2003*] Y. Jin, G-A. Luo, “Numerical calculation of the electroosmotic flow at the cross region in microfluidic chips”, Electrophoresis (2003) 24:1242-1252.

[*Jones, 1995*] T.B. Jones, “Electromechanics of particles”, Cambridge University Press, 1995.

[*Krishnan et al., 2007*] M. Krishnan, I. Monch, P. Schwille, “Spontaneous stretching of DNA in a two-dimensional nanoslit”, Nano Letters (2007) 5:1270-1275.

[*Kundu and Cohen, 2004*] P.K. Kundu and I.M. Cohen, “Fluid Mechanics”, Elsevier Academic Press, 2004.

[*Kutchoukov et al., 2004*] V.G. Kutchoukov, F. Laugere, W. van der Vlist, L. Pakula, Y. Garini, A. Bossche, “Fabrication of nanofluidic devices using glass-to-glass anodic bonding”, Sensors and Actuators A (2004) 114:521-527.

[*Landau and Lifshitz, 2004*] L.D. Landau and E.M. Lifshitz, “Fluid Mechanics”, Elsevier Butterworth-Heinemann, 2004.

[*Laurell et al., 2004*] T. Laurell, J. Nilsson, K. Jensen, D.J. Harrison and J.P. Kutter (eds.), Proceedings of MicroTAS, 2004.

[*Li, 2004*] D. Li, “Electrokinetics in Microfluidics”, Elsevier Ltd., 2004.

[*Lin et al., 2002*] J.Y. Lin, L.M. Fu, R.J. Yang, “Numerical simulation of electrokinetic focusing in microfluidic chips”, Journal of Micromechanics and Microengineering (2002) 12:955-961.

[*Luengo et al., 1999*] C.L. Luengo, L.J. van Vliet, B. Rieger, M. van Ginkel, DIPimage: a scientific image processing toolbox for Matlab Delft University of Technology, 1999, http://www.qi.tnw.tudelft.nl/DIPlib/

[*Manz et al., 1990*] A. Manz, N. Graber, H.M. Widmer, “Miniaturized total chemical analysis systems: A novel concept for chemical sensing”, Sensors and Actuators B (1990) 1:244-248.

[*Markesteijn et al., 2006*] A.P. Markesteijn, G.O.F. Parikesit, Y. Garini, and J. Westerweel, “Numerical simulation of electroosmotic flow in complex micro- and nanochannels”, Proceedings of the Second International

Conference on Transport Phenomena in Micro and Nanodevices, Il Ciocco Hotel and Conference Center, Barga, Italy, 11-15 June 2006.

[*Mazo, 2002*] R.M. Mazo, “Brownian Motion: Fluctuations, Dynamics, and Applications”, Oxford Science Publications, 2002.

[*Meagher et.al., 2005*] R. J. Meagher, J-I. Won, L.C. McCormick, S. Nedelcu, M.M. Bertrand, J.L. Bertram, G. Drouin, A.E. Barron, G.W. Slater, “End-labeled free-solution electrophoresis of DNA”, Electrophoresis (2005) 26:331-350.

[*Mitchell et al., 2000*] M.J. Mitchell, R. Qiao, N.R. Aluru, “Meshless Analysis of Steady-State Electroosmotic Transport”, Journal of Microelectromechanical Systems (2000) 9:435-449.

[*Murphy, 2001*] D.B. Murphy, “Fundamentals of light microscopy and electronic imaging”, Wiley-Liss, Inc., 2001.

[*Nguyen and Wereley, 2002*] N.T. Nguyen and S.T. Wereley, “Fundamentals and Applications of Microfluidics”, Artech House Inc., 2002.

[*Parikesit et al., 2004*] G.O.F. Parikesit, V.G. Kutchoukov, A. Bossche, I.T. Young, Y. Garini, “Optical detection of single molecules in nanofluidic chips”, Proc. of SPIE (2004) 5718:133-141.

[*Parikesit et al., 2005*] G.O.F. Parikesit, A.P. Markesteijn, V.G. Kutchoukov, O.M. Piciu, A. Bossche, J. Westerweel, Y. Garini, I.T. Young, “Electroosmotic flow analysis of a branched U-turn nanofluidic device“, Lab on a Chip (2005) 5:1067-1074.

[*Parikesit et al., 2007a*] G.O.F. Parikesit, A.P. Markesteijn, J. Westerweel, I.T. Young, Y. Garini, “Free-Flow Dielectrophoresis – A Numerical Study“, Proceedings of MicroTAS (2007).

[*Parikesit et al., 2007b*] G.O.F. Parikesit, A.P. Markesteijn, O.M. Piciu, A. Bossche, J. Westerweel, I.T. Young, Y. Garini, “Size-dependent electrokinetic pathlines of DNA molecules in sieve-less U-turn nanochannels“, submitted (2007).

[*Parikesit, 2008*] G.O.F. Parikesit, “Fluorescence measurements”, in Encyclopedia of Microfluidics and Nanofluidics (editor: Dongqing Li), Springer, in press.

[*Patankar et al., 1998*] N.A. Patankar, H.H. Hu, “Numerical simulation of electroosmotic flow”, Analytical Chemistry (1998) 70:1870-1881.

[*Pennathur et al., 2005*] S. Pennathur, J.G. Santiago, “Electrokinetic transport in nanochannels. 2. Experiments”, Analytical Chemistry (2005) 77:6782-6789.

[*Pennathur et al., 2007*] S. Pennathur, F. Baldessari, M. Kattah, P.J. Utz, J.G. Santiago, “Free-solution oligonucleotide separation in nanoscale channels”, Analytical Chemistry, accepted (2007).

[*Petersen et.al., 2007*] E. Petersen, B. Li, X. Fang, H. Luo, V. Samuilov, D. Gersappe, J. Sokolov, B. Chu, M. Rafailovich, "DNA migration and separation on surfaces with a microscale dielectrophoretic trap array", Physical Review Letters (2007) 98:088102.

[*Pohl, 1978*] H.A. Pohl, “Dielectrophoresis - The behaviour of neutral matter in nonuniform electric fields”, Cambridge University Press, 1978.

[*Pratt and Cornely, 2004*] C.W. Pratt, K. Cornely, “Essential Biochemistry”, John Wiley and Sons, Inc., 2004.

[*Probstein, 2003*] R.F. Probstein, “Physicochemical hydrodynamics – An Introduction”, John Wiley and Sons, Inc., 2003.

[*Purcell, 1977*] E.M. Purcell, “Life at low Reynolds number”, American Journal of Physics (1977) 45:3-11.

[*Qu et al., 2000*] W. Qu, D. Li, “A Model for Overlapped EDL Fields”, J. Colloid Interface Sci. (2000) 224:397-407.

[*Regtmeier et.al., 2007*] J. Regtmeier, T.T. Duong, R. Eichhorn, D. Anselmetti, A. Ros, "Dielectrophoretic manipulation of DNA: Separation and polarization", Analytical Chemistry (2007) 79:3925-3932.

[*Rice et al., 1965*] C.L. Rice, R. Whitehead, “Electrokinetic Flow in a Narrow Cylindrical Capillary”, Journal of Physical Chemistry (1965) 69:4017-4024.

[*Riehn et.al., 2006*] R. Riehn, R.H. Austin, J.S. Sturm, "A nanofluidic railroad switch for DNA", Nano Letters (2006) 6:1973-1976.

[*Rubinstein and Colby, 2003*] M. Rubenstein, R.H. Colby, “Polymer Physics”, Oxford University Press, 2003.

[*Rye et al., 1992*] H.S. Rye, S. Yue, D.E. Wemmer, M.A. Quesada, R.P. Haugland, R.A. Mathies, A.N. Glazer, “Stable fluorescent complexes of double-stranded DNA with bis-intercalating asymmetric cyanine dyes: properties and applications”, Nucleic Acids Research (1992) 20:2803-2812.

[*Santiago, 2001*] J.G. Santiago, “Electroosmotic Flows in Microchannels with Finite Inertial and Pressure Forces”, Analytical Chemistry (2001) 73:2353-2365.

[*Sinton, 2004*] David Sinton, “Microscale flow visualization”, Microfluidics and Nanofluidics (2004) 1:2-21.

[*Squires et al., 2005*] T.M. Squires, S.R. Quake, “Microfluidics: Fluid physics at the nanoliter scale”, Reviews of Modern Physics (2005) 77:977-1026.

[*Stavis et al., 2004*] S.M. Stavis, J.B. Edel, K.T. Samiee, H.G. Craighead, “Single molecule studies of quantum dot conjugates in a submicrometer fluidic channel”, Lab on a Chip (2004) 5:337-343.

[*Striemer et.al., 2007*] C.C. Striemer, T.R. Gaborski, J.L. McGrath, P.M. Fauchet, "Charge- and size-based separation of macromolecules using ultrathin silicon membranes", Nature (2007) 445:749-753.

[*Takamura et al., 2003*] Y. Takamura, H. Onoda, H. Inokuchi, S. Adachi, A. Oki, Y. Horiike, “Low-voltage electroosmosis pump for stand-alone microfluidics devices”, Electrophoresis (2003) 24:185-192.

[*Tegenfeldt et al., 2004*] J.O. Tegenfeldt, C. Prinz, H. Cao, R.L. Huang, R.H. Austin, S.Y. Chou, E.C. Cox, J.C. Sturm, “Micro- and nanofluidics for

DNA analysis", Analytical and Bioanalytical Chemistry (2004) 378:1678–1692.

[*Tretheway et al., 2002*] D.C. Tretheway, C.D. Meinhart, "Apparent fluid slip at hydrophobic microchannel walls", Physics of Fluids (2002) 14:L9-L12.

[*Venter et al., 2001*] J.C. Venter et.al., "The sequence of the human genome", Science (2001) 291:1304-1351.

[*Verwey and Overbeek, 1948*] E.J.W. Verwey, J.Th.G. Overbeek, "Theory of the Stability of Lyophobic Colloids", Elsevier, 1948.

[*Viovy, 2000*] J-L. Viovy, "Electrophoresis of DNA and other polyelectrolytes: Physical mechanisms", Reviews of Modern Physics (2000), 72:813-872.

[*Wang et al., 2004*] Z. Wang, J. El-Ali, M. Engelund, T. Gotsaed, I.R. Perch-Nielsen, K.B. Mogensen, D. Snakenborg, J.P. Kutter, A. Wolff, "Measurements of scattered light on a microchip flow cytometer with integrated polymer based optical elements", Lab on a Chip (2004), 4:372-377.

[*Westerweel et al., 2004*] J. Westerweel, P.F. Geelhoed, R. Lindken, "Single-pixel resolution ensemble correlation for micro-PIV applications", Experiments in Fluids (2004) 37:375-384.

[*Whitesides, 2006*] G. Whitesides, "The origins and the future of microfluidics", Nature (2006) 42:368-373.

[*Yamada et al., 2006*] M. Yamada, M. Seki, "Microfluidic particle sorter employing flow splitting and recombining", Analytical Chemistry (2006) 78:1357-1362.

[*Yang et al., 2001*] R.J. Yang, L.M. Fu, Y.C. Lin, "Electroosmotic flow in microchannels", Journal of Colloid and Interface Science (2001) 239:98-105.

[*Yao et al., 2003*] S. Yao, J.G. Santiago, "Porous glass electroosmotic pumps: theory", Journal of Colloid and Interface Science (2003) 268:133-142.

[*Young et al., 1998*] I.T. Young, J.J. Gerbrands, L.J. van Vliet, "Image Processing Fundamentals", Chapter 51 of The Digital Signal Processing Handbook, CRC Press LLC, 1998.

[*Zander et al., 2002*] Ch. Zander, J. Enderlein, R.A. Keller (eds.), "Single molecule detection in solution – Methods and applications", Wiley-VCH, 2002.

List of symbols

	Definition	**Units**
A	Amplitude of AC electric field	V = m^{2} kg s^{-3} A^{-1}
B	Amplitude of DC electric field	V = m^{2} kg s^{-3} A^{-1}
D	Brownian diffusion coefficient	m^{2} s^{-1}
d	Mean Brownian displacement	m
E	Electric field vector	V/m = m kg s^{-3} A^{-1}
e	The charge of an electron; 1.60217653(14) × 10^{-19}	s A
f	Frequency of AC electric field	Hz = s^{-1}
F	Correction factor in Henry equation	-
h	Channel depth	m
K	Clausius-Mossoti (CM) function	-
k_b	Boltzmann constant; 1.3806505(24) × 10^{-23}	J/K = m^{2} kg s^{-2} K^{-1}
l	Characteristic length (in Reynolds number)	m
M	Salt molarity in fluid	mol m^{-3}
N_a	Avogadro number; 6023 x 10^{23}	mol^{-1}
n	Number of images in measured electro-osmosis	-
n_i	Ionic number concentration of ions of type i (i.e. n_+ or n_-)	m^{-3}
n_∞	Ionic number concentration of the bulk liquid	m^{-3}
P	Hydrostatic pressure	Pa = m^{-1} kg s^{-2}
p	Dipole moment vector	s A m
q_p	Net charge between a particle and the counter-ions in its electric double-layer	C = s A
r_p	Particle radius	m
R	Reynolds number	-
R_g	Radius-of-gyration of a DNA molecule	m
r_{start}	Start distance in DNA analysis	m
r_{finish}	Finish distance in DNA analysis	m
T	Absolute temperature	K
t	Time	s
u	Bulk fluid velocity	m s^{-1}
V	Electric voltage	V = m^{2} kg s^{-3} A^{-1}
ΔV_{EO}	Applied external electric potential in electro-osmosis	V = m^{2} kg s^{-3} A^{-1}
v	Velocity vector	m s^{-1}

v_D	Velocity deviation in electro-osmosis analysis	$m\ s^{-1}$
v_M	Measured velocity in electro-osmosis analysis	$m\ s^{-1}$
v_S	Simulated velocity in electro-osmosis analysis	$m\ s^{-1}$
v_{EO}	Electro-osmotic velocity	$m\ s^{-1}$
v_{EP}	Electrophoretic velocity	$m\ s^{-1}$
v_{DEP}	Dielectrophoretic velocity	$m\ s^{-1}$
Z	The absolute value of the ionic valence	-
Z_i	The absolute value of the ionic valence of ions type *i* (i.e. n_+ or n_-)	-
γ	Surface tension	$kg\ s^{-2}$
ε	Relative permittivity of liquid solution	-
ε_0	Permittivity of vacuum	$m^{-3}\ kg^{-1}\ s^4\ A^2$
ε_l	Relative permittivity of liquid solution (in dielectrophoresis)	-
ε_s	Relative permittivity of a sphere (in dielectrophoresis)	-
ζ	Zeta potential (electrical potential at the shear plane in the electric-double layer)	$V = m^2\ kg\ s^{-3}\ A^{-1}$
ζ_p	Zeta potential in beads	$V = m^2\ kg\ s^{-3}\ A^{-1}$
κ	Debye-Huckel parameter	m^{-1}
μ	Dynamic fluid viscosity	$m^{-1}\ kg\ s^{-1}$
μ_{EK}	Electro-osmotic-plus-electrophoretic mobility	$kg\ s^{-2}\ A^{-1}$
μ_{DEP}	Dielectrophoretic mobility	$m\ kg^2\ s^{-5}\ A^{-2}$
v	Kinematic fluid viscosity	$m^2\ s^{-1}$
ρ	Fluid density	$m^{-3}\ kg$
ρ_e	Local net charge density	$s\ A\ m^{-3}$
ρ_μ	Ratio of dielectrophoretic mobility and electro-osmotic-plus-elektrokinetic mobility	$m\ kg\ s^{-7}\ A^{-3}$
ψ	Local electric field potential in liquid solution	$V = m^2\ kg\ s^{-3}\ A^{-1}$

Acknowledgements

This work is done at the Quantitative Imaging (QI) group –formerly known as the Pattern Recognition (PH) group– in Delft University of Technology, officially since 1 November 2003. First and foremost, I thank my supervisors Ted Young and Yuval Garini (who is now in Bar-Ilan University, Israel) who trustingly gave the necessary freedom and feedbacks, kindly nurtured my skills, and actively support my personal planning (e.g. by approving my plan to finish this PhD Project within my 4-year employment contract and by supporting my intention to find a Post-Doc position in Delft that allows me to both further advance my research career and to live together with my wife and daughter). At the QI group I enjoyed the knowledge, jokes, and C++'s shared by my lab-mates (Heidi Dietrich, Margreet Docter, Bart Vermolen, Sanneke Brinkers), room-mates (Martijn van de Giessen, Kees van Wijk, Simona Grigorescu, Tuan Pham, Bernd Rieger), support team (Ronald Ligteringen, Wouter Smaal, Mandy Jungschlager, Wim van Oel, Guus Liqui Lung, Klara Schaafsma), and all my other group-mates, including Suprijanto, my teacher in Bandung who became my colleague in the group.

I also benefit from collaborations with other groups in Delft: the Electronic Instrumentation laboratory (Oana Piciu, Vladimir Kutchoukov, Lujun Zhang, Andre Bossche), the laboratory for Aero and Hydrodynamics (Anton Markesteijn, Ralph Lindken, Jerry Westerweel), and the Molecular Biophysics group (Derek Stein, Frank van der Heyden, Christine Meyer, Cees Dekker). I acknowledge discussions I had with other colleagues during all the conferences and courses I attended. I am grateful for financial support by Stichting FOM and for all feedbacks from my Examination Committee (Professors Jerry Westerweel, Cees Dekker, Hans Tanke, Menno Prins, Albert van den Berg, and Lucas van Vliet). I thank both Indraswari Kusumaningtyas and Aura Mimosa Nugrowati for meticulously proof-reading this manuscript. I also thank all my Indonesian friends who help to make me feel at home in Delft. I am very much indebted to the education given by all my mentors and teachers in Delft and in Bandung.

I personally dedicate this work to my beloved family: my late mother Laksmi Nugrowati Soehargo, who have always taught me with her exuberant spirit to never stop learning and sincerely doing my best; my father Parikesit Iskandar Abdoel Charnen, who have always relentlessly supported me to get all my education and showed me the virtue of patience; my sister Aura Mimosa Nugrowati, who is always my best friend and rival ever since she was born; my father-in-law Subagio, mother-in-law Budi Astuti, and brother-in-law Indrasatya Kusumajati, with their immense trust and encouragements; the big Soehargo family with their cheerful and heartfelt support; my daughter Naureen Hanifa Parikesit, who is the brightest light and inspiration in my life; and my wife Indraswari Kusumaningtyas, my soulmate and lifelong partner, with whom I share my dreams, joy, and sorrow. I am deeply grateful to ALLAH for everything. All praises be to HIM, the Most Beneficent, the Most Merciful, the source of all love and knowledge.

Gea O.F. Parikesit, Delft, January 2008

Curriculum Vitae

Gea Oswah Fatah Parikesit was born on November 24th, 1978, in Bandung, Indonesia. He studied in St. Yusuf Primary School (1984-1990) and St. Aloysius Secondary Schools (1990-1996) before joining the Engineering Physics undergraduate program in *Institut Teknologi Bandung* (ITB). In 1999-2000 he worked as a Teaching Assistant for the courses ‘Fluid Mechanics’, ‘Acoustics’, ‘Measurements’, ‘Heat and Mass Transfer’, ‘Thermal Analysis’, ‘Electronics’, and ‘Laser and Fiber Optics’. In 2001 he performed his final year project “Design and Fabrication of an Articulated Arm as a Low-Power Laser Beam Delivery Device” at the Laboratory of Optics under supervision of Prof. A. Handojo and Dr. E. Juliastuti.

In 2001-2003, Gea obtained the STUNED scholarship and enrolled in the MSc International Program of Applied Physics in *Technische Universiteit Delft* (TUD) in The Netherlands. He finished his MSc research “Laser Frequency Stabilization for Multiple-Wavelength Interferometer” at the Optics Research Group under supervision of Prof. J.J.M. Braat and Dr. M.L. Krieg. Related to this thesis, in the summer of 2002 he had an internship in *Nederlands Meet-instituut* (NMi) on the subject “Laser Frequency Digital Stabilization for A Portable and User-Friendly Optical Frequency Standard”.

From November 2003 until October 2007, Gea was employed as a Junior Researcher at the Quantitative Imaging group in TUD under supervision of Prof. I.T. Young and Dr. Y. Garini. He performed research in the project “Nanoscale Electrophoresis”, funded by *Stichting voor Fundamenteel Onderzoek der Materie* (FOM), the result of which is published as this thesis. In the same period, he was involved in teaching the laboratory class ‘Physics Instrumentation’. Since November 2007, Gea is employed as a Post-doctorate Researcher at the Laboratory for Aero and Hydrodynamics in TUD under supervision of Prof. J. Westerweel and Dr. R.H. Lindken, where he will continue using optical methods and digital image analysis to investigate flows at the nanometer scale.

Gea’s research is mainly in optics and microfluidics. Gea is married to Indraswari Kusumaningtyas since July 2004. Together with their daughter, Naureen Hanifa Parikesit, they are presently living in Delft. More on this family can be found at their webpage: http://gea.ari.googlepages.com/

Propositions

with the thesis
Nanofluidic electrokinetics in quasi-two-dimensional branched U-turn channels
Gea Oswah Fatah PARIKESIT, Delft University of Technology,
Monday 14 January 2008.

1. Continuous length-based separation of DNA molecules without a sieving matrix can be performed in nanochannels.
2. Scientists are sometimes forced to choose technological solutions instead of scientific solutions.
3. To discern moving-objects from their background, humans rely more on motion-detection schemes than on intensity-based segmentation.
4. When scientists consider scientific discoveries as the absolute truth, they no longer differentiate between science and religion.
5. People publish scientific papers with two kinds of intentions: (1) to show off to the society, and / (or) (2) to share the results with society.
6. In order to defend a PhD thesis in a scholarly manner, a PhD candidate needs to maintain a thinking rate that is at least twice as fast as his/her talking rate.
7. When someone is able to think of his/her rights as privileges, then one is able to exercise these rights in a responsible and considerate manner.
8. Prejudice and ignorance are basic human survival mechanisms, which ironically hinder humans from learning as fast as they should.
9. The month-age of a newborn baby determines the parents' sleeping-hours distribution more than it determines the parents' number of sleeping-hours.
10. The worst procrastination is to discuss what the worst procrastination is.

These propositions are considered opposable and defendable and as such have been approved by the supervisors, Prof. dr. I.T. Young and Prof. dr. Y. Garini.

Stellingen

behorende bij het proefschrift
Nanofluidic electrokinetics in quasi-two-dimensional branched U-turn channels
Gea Oswah Fatah PARIKESIT, Technische Universiteit Delft,
Maandag 14 Januari 2008.

1. De ononderbroken lengte-gebaseerde scheiding van DNA molekulen zonder een zeven matrijs kan in nano-kanalen worden gedaan.
2. Wetenschappers worden soms gedwongen om technologische oplossingen in plaats van wetenshappelijke oplossingen te kiezen.
3. Om bewegen-voorwerpen van hun achtergrond te onderscheiden, baseren de mensen zich meer op beweging-ontdekking regelingen dan bij de op intensiteit-gebaseerde segmentatie.
4. Wanneer wetenschappers wetenschappelijke ontdekkingen als de absolute waarheid beschouwen, onderscheiden zij niet meer tussen wetenschap en religie.
5. Mensen publiceren wetenschappelijke documenten met twee soorten van intenties: (1) aan de maatschappij opscheppen, en / (of) (2) om de resultaten met de maatschappij te delen.
6. Om een proefschrift op een geleerde manier te verdedigen, moet een promovendus een denk snelheid handhaven dat tenminste tweemaal even snel is als zijn/haar spreek snelheid.
7. Als iemand aan zijn/haar rechten kan denken als voorrechten, dan kan hij/zij die rechten op een verantwoordelijke en attente manier uitoefenen.
8. Vooroordeel en onwetendheid zijn fundamentele menselijke overlevingsmechanismen, die mensen ironisch belemmeren van te leren even snel als zij zou kunnen.
9. De maand-leeftijd van een pasgeboren baby bepaalt de slaap-uren van de ouders distributie meer dan het bepaalt het aantal van de ouders slaap-uren.
10. Het slechtste uitstel is te bespreken wat het slechtste uitstel is.

Deze stellingen worden opponeerbaar en verdedigbaar geacht en zijn als zodanig goedgekeurd door de promotoren, Prof. dr. I.T. Young en Prof. dr. Y. Garini.